

# REPORT DOCUMENTATION PAGE

AFRL-SR-AR-TR-03-

0276

the data needed, and completing and reviewing this collection of information. Send comments regarding this burden estimate or any reducing this burden to Washington Headquarters Services, Directorate for Information Operations and Reports, 1215 Jefferson Davis Management and Budget, Paperwork Reduction Project (0704-0188), Washington, DC 20503

1. AGENCY USE ONLY (Leave blank)		2. REPORT DATE	3. REPORT TYPE AND DATES COVERED Final Report 11/13/99 - 11/14/02	
4. TITLE AND SUBTITLE Turbulence Modeling Using Body Force Potentials			5. FUNDING NUMBERS F49620-00-1-0033	
6. AUTHOR(S) Blair Perot				
7. PERFORMING ORGANIZATION NAME(S) AND ADDRESS(ES) University of Massachusetts Office of Grants and Contracts Amherst MA, 01003			8. PERFORMING ORGANIZATION REPORT NUMBER	
9. SPONSORING / MONITORING AGENCY NAME(S) AND ADDRESS(ES) AFOSR Tom Beutner 4015 Wilson Blvd., Rm 713 Arlington, VA 22203-1954			10. SPONSORING / MONITORING AGENCY REPORT NUMBER	
11. SUPPLEMENTARY NOTES				
12a. DISTRIBUTION / AVAILABILITY STATEMENT  <b>Approved for public release; distribution unlimited.</b>			12b. DISTRIBUTION CODE	
<p>13. ABSTRACT (Maximum 200 Words)</p> <p>The objective of this study was the development and testing of the turbulent potential model in complex non-equilibrium flows. The initial emphasis was on evaluating and enhancing the models performance in rotating flows and in transition to turbulence. The project was extended in the third year to examine the model's ability to act as a subgrid scale model in Large Eddy Simulations (LES).</p> <p>The turbulent potential model is an alternative approach to Reynolds Averaged Navier-Stokes (RANS) turbulence modeling, where the primary quantity of interest is no longer the Reynolds stress tensor. Instead the divergence of the Reynolds stress tensor, a body force vector, is the primary quantity describing how the turbulence affects the mean flow evolution. The potential model approach does not hypothesize any explicit relationship between the turbulence and the mean flow, it is therefore capable of capturing non-equilibrium turbulent flows, and is physically equivalent to Reynolds stress transport (RST) models. However, because the focus is on a vector quantity rather than a tensor, the model equations for the turbulent potential model are simpler than RST models and roughly comparable in cost and complexity to the widely used two equation models.</p>				
14. SUBJECT TERMS			15. NUMBER OF PAGES 48	
			16. PRICE CODE	
17. SECURITY CLASSIFICATION OF REPORT	18. SECURITY CLASSIFICATION OF THIS PAGE	19. SECURITY CLASSIFICATION OF ABSTRACT	20. LIMITATION OF ABSTRACT	

20030731 107

Professor Blair Perot  
 Department of Mechanical Eng.  
 University of Massachusetts  
 Amherst, MA 01003  
 (413) 545-3925  
 perot@ecs.umass.edu

# Final Report

## *Turbulence Modeling using Body Force Potentials.*

### Objective

The objective of this study was the development and testing of the turbulent potential model in complex non-equilibrium flows. The initial emphasis was on evaluating and enhancing the models performance in rotating flows and in transition to turbulence. The project was extended in the third year to examine the model's ability to act as a subgrid scale model in Large Eddy Simulations (LES).

The turbulent potential model is an alternative approach to Reynolds Averaged Navier-Stokes (RANS) turbulence modeling, where the primary quantity of interest is no longer the Reynolds stress tensor. Instead the divergence of the Reynolds stress tensor, a body force vector, is the primary quantity describing how the turbulence affects the mean flow evolution, and transport equations for the Helmholtz potentials of that body force vector are derived and then closed using modeled transport equations.

The potential model approach does not hypothesize any explicit relationship between the turbulence and the mean flow, it is therefore capable of capturing non-equilibrium turbulent flows, and is physically equivalent to Reynolds stress transport (RST) models. However, because the focus is on a vector quantity rather than a tensor, the model equations for the turbulent potential model are simpler than RST models and roughly comparable in cost and complexity to the widely used two equation models.

## 1. Potential Model

### 1.1 Turbulence Body Force Potentials

Turbulence potentials were introduced by Perot (1996), and are related to the Reynolds stress tensor,  $\mathbf{R}$ , through the following relationship

$$\nabla \cdot \mathbf{R} = \nabla \times \boldsymbol{\Psi} + \nabla \phi \quad (1.1)$$

$\boldsymbol{\Psi}$  is a vector, and  $\phi$  is a scalar. They can be regarded as potentials because their curl and gradient give a body force. The following relationship is chosen to ensure that the potentials are unique

$$\nabla \cdot \boldsymbol{\Psi} = 0 \quad (2.1)$$

The physical meaning of the turbulent potentials is explained by Perot and Moin (1996).  $\phi$  can be interpreted as a pressure created due to the turbulence. The vector potential can be interpreted as the average vorticity in turbulent filaments. If the eddy viscosity hypothesis is used then  $\boldsymbol{\Psi}$  can be shown to be equal to an eddy viscosity multiplied by the mean vorticity. In the actual model, the eddy viscosity hypothesis is not used and a transport equation for the vector potential is solved.

The turbulent potentials are related to  $\mathbf{R}$  by the following equations

$$\nabla^2 \phi = \nabla \cdot (\nabla \cdot \mathbf{R}) \quad (1.3)$$

$$\nabla^2 \psi = -\nabla \times (\nabla \cdot \mathbf{R}) \quad (1.4)$$

which can be obtained by operating on (1.1) with a divergence and with a curl respectively. However, if the flow is inhomogeneous in only one direction in a Cartesian coordinate system, then we can obtain a one-to-one relationship between the relevant components of the turbulent potentials and the Reynolds stresses. Thus if the flow is inhomogeneous in only the  $y$  direction ( $x_2$  in Cartesian tensor notation), then (1.3) and (1.4) will reduce to

$$\phi_{,22} = R_{22,22} \quad (1.5)$$

$$\psi_{1,22} = -R_{23,22} \quad (1.6)$$

$$\psi_{2,22} = 0 \quad (1.7)$$

$$\psi_{3,22} = R_{12,22} \quad (1.8)$$

Now, if we assume that the turbulent potentials vanish when the turbulence vanishes, then we have, from (1.5) to (1.8),

$$\phi = R_{22} \quad , \quad \psi_1 = -R_{32} \quad , \quad \psi_2 = 0 \quad , \quad \psi_3 = R_{12} \quad (1.9)$$

Flows with inhomogeneity in one direction include fully developed channel flows, fully developed spanwise rotating channel flows, fully developed streamwise rotating channel flows, and (to a some degree) 2D and 3D boundary layers and free shear flows.

## 1.2 The Potential Model Transport Equations

The potential model is a set of transport equations for the turbulent potentials and two auxiliary variables ( $k$  and  $\epsilon$ ) used to model the source terms in those transport equations. The auxiliary variables are not used to model the turbulence effects on the mean flow so this model is not close to a standard  $k/\epsilon$  model. The equations, their derivation, and the rationale for the model is an extensive topic, that was completed prior to this project and presented in Perot (1999). This work also uses the model to calculate rotating channel flow, a mixing layer, adverse pressure gradient boundary layer and the flow over a backward facing step. The results are all in good accord with corresponding DNS, LES or experimental data. Some more practical engineering flows like the flow due to an impinging jet were successfully simulated by Wang (2000). The applications of the model to 3D boundary layer and rotating turbulent flows were studied by Are (2001) and Bhattacharya (2002) respectively. More recently, Zhang (2002) applied the model with an unstructured staggered mesh scheme to simulate the unsteady vortex shedding in flows over two-dimensional obstacles and Wang (2002) has evaluated the model's ability to predict transition. The work of Wang and Bhattacharya were funded by this project and is presented below.

The turbulent potential model is given by the following equations.

$$\frac{D\phi}{Dt} = \nabla \cdot (v + v_t) \nabla \phi + \Pi_\phi^{slow} + \Pi_\phi^{rapid} - \varepsilon_\phi + C_i \left(1 - 1.5 \frac{\phi}{k}\right) P \left(\frac{v_t}{v}\right)^{1/2} \quad (1.10)$$

$$\frac{D\psi}{Dt} = \nabla \cdot (v + v_t) \nabla \psi + \Pi_\psi^{slow} + \Pi_\psi^{rapid} - \varepsilon_\psi + C_i \left(\frac{v_t}{v}\right)^{1/2} \omega k + \frac{k}{\varepsilon} \mathbf{A} \quad (1.11)$$

$$\frac{Dk}{Dt} = \nabla \cdot (v + v_t \bar{\sigma}_k) \nabla k + P - \varepsilon \quad (1.12)$$

$$\frac{D\varepsilon}{Dt} = \nabla \cdot (v + v_t \bar{\sigma}_\varepsilon) \nabla \varepsilon + C_r \frac{\hat{\varepsilon}}{k} (C_{\varepsilon 1} P - C_{\varepsilon 2} \varepsilon) \quad (1.13)$$

Constants and parameters are given by:

$$P = \psi \cdot \mathbf{s}, \quad v_t = 0.21 \frac{\phi k}{\hat{\varepsilon}}, \quad \alpha = \frac{1}{1 + \frac{3}{2} \frac{\phi}{k}}, \quad \xi = |\hat{\omega}| \frac{k}{\hat{\varepsilon}}, \quad q = -2\gamma(2\alpha - 1)(1 - 0.7\gamma)$$

$$\hat{\varepsilon} = \varepsilon / [1 + 10\nu |\nabla k|^{1/2} |k|]$$

$$C_{p1} = 2.0 \frac{v_t}{v_t + 10\nu}, \quad C_i = 0.0033, \quad C_r = \frac{(1 + 0.105\xi)}{(1 + 0.06\xi)} \quad (1.14)$$

$$C_{p2}^S = 0.6 + 0.3 \frac{P\alpha}{\varepsilon} + 1.4(2\alpha - 1), \quad C_{p2}^W = \frac{\phi}{k} (0.6 - C_{p2}^S) + C_{p2}^S$$

$$\sigma_k = 0.33 + 0.67P / \hat{\varepsilon}$$

$$\sigma_\varepsilon = 0.33 + 0.5P / \hat{\varepsilon}$$

$$C_{e1} = 1.45, \quad C_{e2} = 1.83 - 0.16 \exp\left(-0.25 \frac{k^2}{\nu \varepsilon}\right)$$

$$\mathbf{A} = 0.02 \mathbf{s} \times (\mathbf{s} \times \boldsymbol{\psi}) + 0.15 (\hat{\omega} - \mathbf{s}) \times ((\hat{\omega} - \mathbf{s}) \times \boldsymbol{\psi})$$

The slow pressure strain models are

$$\begin{aligned} \Pi_\phi^{slow} = & -(v + 2v_t) \nabla \left(\frac{\phi}{k}\right) \cdot \nabla k + C_{p1} \frac{\hat{\varepsilon}}{k} (2\alpha - 1) \phi \\ & + (C_{p2} + C_{p4}) \cdot \left[ \frac{\left(\frac{\psi}{k}\right) \left(\frac{\psi}{k}\right)}{v_t / k \left(1 + 25 / \text{Re}\right)} - P / k \right] \phi \end{aligned} \quad (1.15)$$

$$\Pi_{\psi}^{slow} = -(\nu + 2\nu_t) \nabla \left( \frac{\psi}{k} \right) \cdot \nabla k - C_{p1} \frac{\hat{\epsilon}}{k} (1 - \alpha) \psi$$

The fast pressure strain models are

$$\Pi_{\phi}^{rapid} = (2 - C_{p2}^S) \left( P - \frac{P}{k} \phi \right) - (2 - C_{p2}^W) (\psi \cdot \hat{\omega}) \quad (1.16)$$

$$\Pi_{\psi}^{rapid} = (2 - C_{p2}^S) (1 - q) \phi s_i - (2 - C_{p2}^W) q (\phi \hat{\omega}_i) - \frac{\phi}{k} s_i$$

The dissipation terms are given by

$$\varepsilon_{\phi} = 2\nu \nabla \phi^{1/2} \cdot \nabla \phi^{1/2} + 2\alpha \frac{\phi}{k} \varepsilon \quad (1.17)$$

$$\varepsilon_{\psi} = \alpha \frac{\psi}{k} \varepsilon.$$

The vector  $\mathbf{A}$  appears only in 3-D flows, and therefore contributes in predicting the cases of the swirling pipe flow and streamwise rotating channel flow. The terms involving  $C_i$  are the transition terms. With typical values of this constant these terms have no effect on fully turbulent flows. In the presentation above, the rapid pressure terms also contain the production terms since they are closely related.

## 2. Rotation

### 2.1 Background

Rotation occurs in many turbulent flows, and is a critical aspect of such devices and flows as pumps, turbines, and trailing vortices. Turbulence is insensitive to linear accelerations but not rotational ones (a spinning top has the same transformation characteristics). Centrifugal and Coriolis effects have both direct and indirect effects on the turbulence evolution. The complexity of how rotation influences turbulence evolution can be seen even in the simplest turbulent flows. The decay of isotropic turbulence is inhibited when the fluid is strongly rotated. Consequently, high turbulence levels can persist for a much longer time when the fluid is spinning (such as in the core of a trailing vortex). However, while the turbulent kinetic energy remains large, the influence of the turbulence on the mean flow (shear stress) actually decreases compared to a non-rotating flow. The core of trailing vortex behaves as if it was laminar (not influenced by turbulence).

These experimental results indicate that simple turbulence models (two equation models, eddy viscosity models) will have a very difficult time modeling rotating turbulence. Mathematically, it can also be shown that the turbulent kinetic energy alone is not a sufficient descriptor of the turbulence when rotation is present. The more complex Reynolds stress transport (RST) models appear to be the simplest turbulence models that are physically rich enough to be able to capture rotation. These models contain explicit and exact Coriolis terms, as well as some rotational terms which need to be modeled.

The turbulent potential model is essentially a reduced (less expensive) RST model. It is expected therefore that this model will also be able to capture rotating turbulent flows reasonably well. However, the slight disadvantage of the potential model approach is that the Production and Coriolis terms are only exact in flows with a single Cartesian inhomogeneous direction. This is apparently the price to be paid for the

reduced cost. In flows with complex inhomogeneity in the turbulence, which frequently is the case in rotating flows, some additional modeling is required over pure RST models.

The modeling of the production and Coriolis terms is described in detail below. The key principal in this modeling effort is the idea that the equations should produce the same answer if you are in a fixed reference frame that sees a rotating mean flow or if you are in a rotating reference frame that moves with the mean flow and therefore has zero mean flow.

## 2.2 Production

The production terms  $\hat{P}_\phi$  and  $\hat{P}_\psi$  have to be modeled in rotating flows. In order to model the production terms, we look at the form of the terms in flows with only one direction of inhomogeneity, and then try to generalize the terms for all flows. We first split the tensor  $\hat{P}_{ij}$  into two parts

$$\hat{P}_{ij} = \hat{P}_{ij}^S + \hat{P}_{ij}^W \quad (2.1)$$

Here

$$\begin{aligned} \hat{P}_{ij}^S &= -R_{ik}S_{jk} - R_{jk}S_{ik} \\ \hat{P}_{ij}^W &= -R_{ik}\hat{W}_{jk} - R_{jk}\hat{W}_{ik} \end{aligned} \quad (2.2)$$

For flows lying in the  $x_1$ - $x_2$  plane with inhomogeneity in only the  $x_2$  direction, we therefore write

$$\begin{aligned} \hat{P}_{12}^S &= -\left(1 + \frac{R_{11}}{R_{22}}\right)R_{22}S_{12} & \hat{P}_{12}^W &= \left(1 - \frac{R_{11}}{R_{22}}\right)R_{22}\hat{W}_{12} \\ \hat{P}_{22}^S &= -2R_{12}S_{12} & \hat{P}_{22}^W &= 2R_{12}\hat{W}_{12} \end{aligned} \quad (2.3)$$

Using the fact that for these kind of flows (1.9) holds, we can then say

$$\begin{aligned} \hat{P}_{\psi_3}^S &= (1 - q(\psi, \phi, k))\phi s_3 & \hat{P}_{\psi_3}^W &= q(\psi, \phi, k)\phi\hat{\omega}_3 \\ \hat{P}_\phi^S &= \psi_3 s_3 & \hat{P}_\phi^W &= -\psi_3\hat{\omega}_3 \end{aligned} \quad (2.4)$$

Where  $q$  is a scalar meant to represent the ratio  $\frac{1}{2}\left(1 - \frac{R_{11}}{R_{22}}\right)$ , which vanishes at isotropy,  $s$  is a vector representing strain and  $\hat{\omega}$  is a vector representing intrinsic vorticity. Now it is easy to see from (2.3) and (2.4) that the vectors have to obey the following relationship with  $\hat{W}$  and  $S$

$$\begin{aligned} \hat{\omega}_3 &= -2\hat{W}_{12} \\ s_3 &= -2S_{12} \end{aligned} \quad (2.5)$$

For 3D flows with inhomogeneity in only the  $x_2$  direction, an additional set of relationships arise

$$\begin{aligned} \hat{\omega}_1 &= 2\hat{W}_{32} \\ s_1 &= 2S_{32} \end{aligned} \quad (2.6)$$

We now try to define  $\hat{\omega}$  and  $s$  more generally so that (2.5) and (2.6) can be satisfied for 3D flows with inhomogeneity in only the  $x_2$  direction. The definition of  $\hat{\omega}$  is quite straightforward

$$\hat{\omega} = \nabla \times \mathbf{v} + 2\Omega \quad (2.7)$$

Which is the same as the intrinsic vorticity defined by Speziale (1989). However, the relationship between  $s$  and the gradients of velocity is not algebraic, and the following equation is solved

$$\nabla^2 (\phi s) = -2\nabla \times \nabla \cdot (\phi \mathbf{S}) \quad (2.8)$$

This equation ensures that  $s$  satisfies the relations (2.5) and (2.6) for the specific case of flows with only one direction of inhomogeneity. However, for general flows, we need to solve for the inverse Laplacian of the source term defined on the right hand side of (2.8). For wall bounded flows,  $\phi$  goes to zero at the wall, and therefore the following boundary condition would be appropriate

$$\phi s|_{\text{wall}} = 0. \quad (2.9)$$

Finally we can define the production terms for the turbulence potentials

$$\begin{aligned} \hat{P}_\phi^S &= \psi_k s_k & \hat{P}_\phi^W &= -\psi_k \hat{\omega}_k & \hat{P}_\phi &= \psi_k s_k - \psi_k \hat{\omega}_k \\ \hat{P}_{\psi_i}^S &= (1 - q(\psi, \phi, k)) \phi s_i & \hat{P}_{\psi_i}^W &= q(\psi, \phi, k) \phi \hat{\omega}_i \\ \hat{P}_{\psi_i} &= (1 - q(\psi, \phi, k)) \phi s_i + q(\psi, \phi, k) \phi \hat{\omega}_i \end{aligned} \quad (2.10)$$

The scalar function  $q$  has been defined in the section defining the model.

### 2.3 Decaying Homogenous Isotropic Turbulence in a Rotating Frame

The prediction of decaying isotropic turbulence in a rotating frame can be used to calibrate the  $k$ - $\epsilon$  equation, more specifically  $C_{\epsilon 2}$ . Experimentally, rotating homogenous isotropic turbulence was produced by Wigeland and Nagib (1978) by setting a uniform flow into solid body rotation as it passed through a honeycomb and a rotating turbulence-generating grid. It has been known that the dissipation rate decreases rapidly due to a disruption of the energy transfer from larger to the smaller scales Speziale (1989).  $C_{\epsilon 2}$  also has a dependence on the Reynolds number as seen by Chasnov (1997). The effect of the Reynolds number and rotation can be seen in (1.14), so that an increase in rotation causes an increase in  $C_r$  while an increase in Reynolds number makes  $C_{\epsilon 2}$  tend to go closer to 1.83.  $C_{\epsilon 2}$  has a lower limit of 1.664 for an initial condition with a  $k^2$  energy spectrum at small wave numbers.

Figure 1 shows the results of the prediction of isotropic decay for 3 cases tried out by Wigeland and Nagib (1978). The x-axis is nondimensional time  $Ut/M$ , where  $U$  is the mean streamwise velocity of the air,  $M$  is the size of the mesh which generates the turbulence, and  $t$  is the time. The y-axis is the nondimensional reciprocal of turbulent kinetic energy  $k_0/k$ , where  $k_0$  is the initial  $k$ . The reciprocal is taken to simply resolve the  $k$  more effectively for different cases.  $Ret = k_0^2/\nu\epsilon_0$ , the initial turbulent Reynolds number, while  $Rot = \epsilon_0/\Omega k_0$ , the initial turbulent Rossby number.

As can be seen from the results, the predictions match quite accurately with the model, and therefore we can say that  $C_{\epsilon 2}$  has been calibrated correctly within the range of Reynolds and Rossby numbers displayed in the figures. The Reynolds number used in later flows are about 10 times larger than what has been used

in these cases. However, it was seen that isotropic decay is more sensitive to lower Reynolds numbers, and is independent of  $Re_t$  for high values of  $Re_t$ .

The effect of Rossby number on the evolution of isotropic turbulence at high Reynolds number can be very clearly seen in the last plot in Figure 1. The model is compared to a high Reynolds number DNS presented in Speziale (1989), and depicts the effect of the rotation dependent factor on the decay of turbulence. The initial turbulent Reynolds number is 390 and the initial turbulent Rossby number is 0.011. The model has been tried with and without the rotation dependent factor  $C_r$  (equation 1.14). Clearly, the presence of  $C_r$  decreases the dissipation rate to the right amount so that the model agrees well with the experiment.

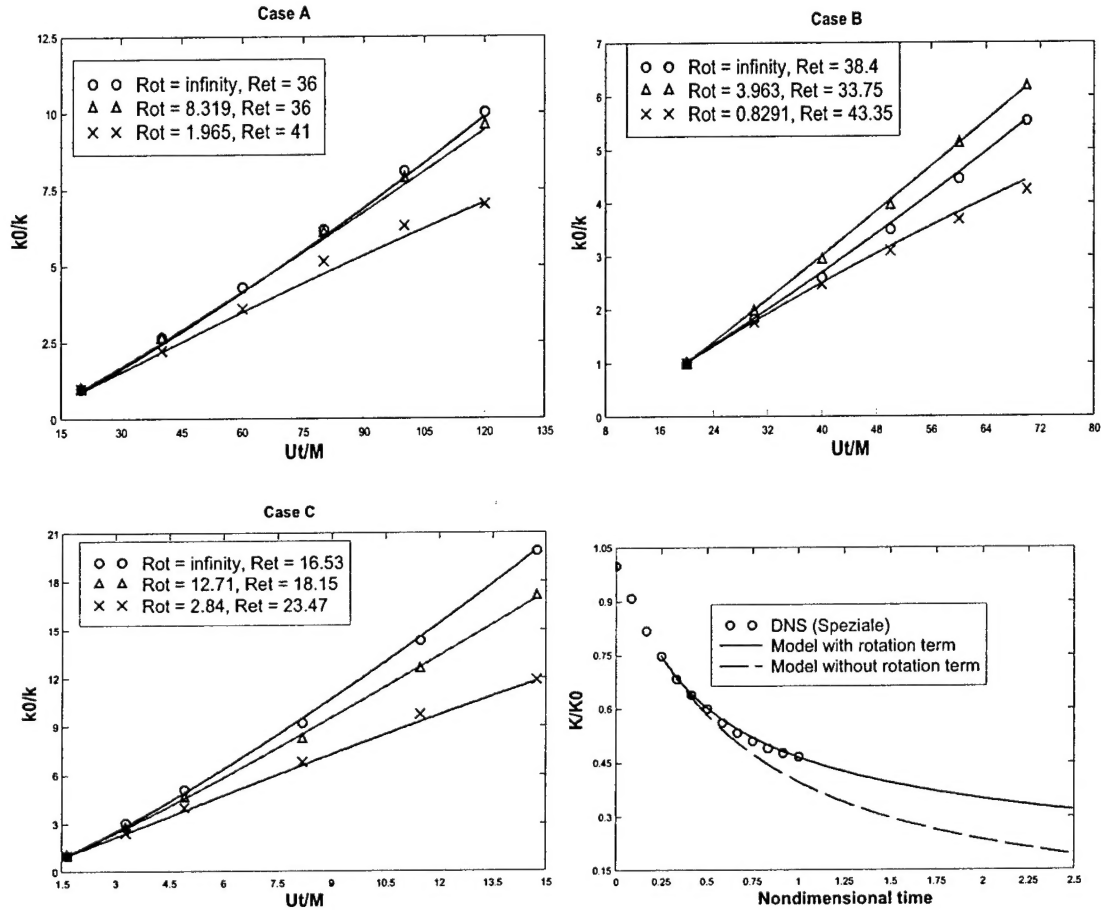


Figure 1. Cases A B and C of Wigeland and Nagib's (1978) experiment. The symbols denote the experiment while lines denote model predictions. Final figure is the DNS results of Speziale at  $Ro=0.011$ .

## 2.4 Rotating Homogenous Planar Shear Flow

In this test case, initially homogenous isotropic turbulence sheared in a plane at a constant rate and a fixed amount of frame rotation is simultaneously superimposed. The rotation is around an axis perpendicular to the plane of the shear. The schematic is shown in Figure 2.



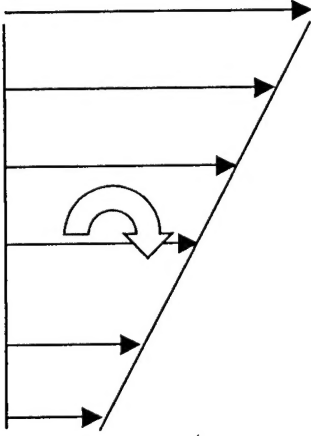


Figure 2. Homogenous shear flow (black arrows) superimposed with frame rotation (block arrow), acting on initially isotropic turbulence. In this figure the shear and the rotation have the same sign.

All the equations come into play, and only terms involving the gradient of turbulence potentials are equal to zero because of the homogeneity. The shear is denoted by  $S = \frac{dv}{dy}$ . The rotation rate by  $\Omega$ . Initially,  $\phi = 0.66k$ ,  $\Psi_3 = 0$ , and  $\epsilon_0/k_0S = 0.25$ .  $\epsilon_0/k_0S$  &  $\Omega/S$  are the only initial condition on which the solution depends, as shown by Speziale & Mac Giolla Mhuiris (1989).

The prediction of homogenous shear flow without frame rotation is compared to DNS data by Matsumoto, Nagano and Tsuji (1991). From Figure 3 we can see that the model predicts a lower turbulent kinetic

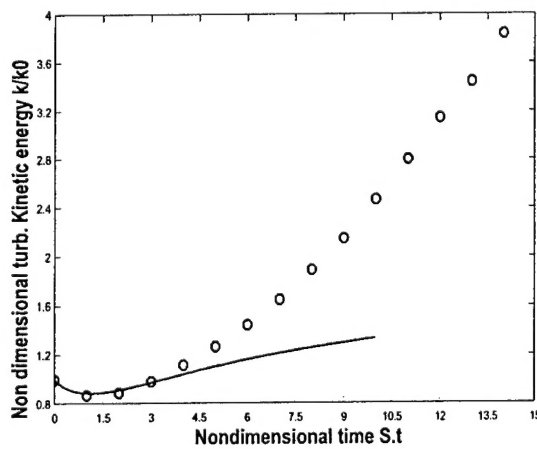


Figure 3. Evolution of turbulent kinetic energy with time for homogenous shear flow with no rotation. Symbols denote DNS data. Line denotes model prediction

energy which seems to be going towards a stable value for large times. The initial evolution does match however, and therefore the value of 0.6 (at isotropy) chosen for  $C_{p2}^s$  is correct.

From Figure 4 we can see that the model agrees reasonably well with the LES for homogenous shear flow with frame rotation, and predicts stable solution for  $\Omega/S=-0.5$ . The turbulent kinetic energy is unstable for a range of  $\Omega/S$  between  $-0.1$  and  $0.65$ , which is higher than the range of  $0 < \Omega/S < 0.5$  predicted by linear stability theory and RDT (Lezius and Johnston, 1976 and Bertoglio, 1982).

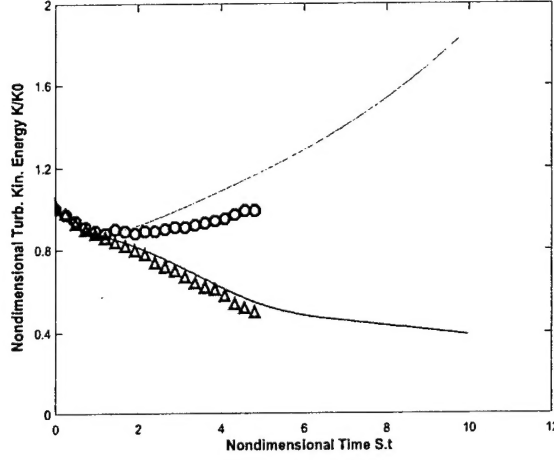


Figure 4. Effect of homogenous shear and rotation on initially isotropic turbulence. Symbols denote LES data of Bardina et al (1983) and lines denote model predictions. The symbol O is for  $\Omega/S=0.5$ ,  $\Delta$  is for  $\Omega/S=-0.5$

Thus the model does not predict the homogenous shear flow very well because it predicts a slow evolution rate for no frame rotation rate. This is of some concern because this evolution rate is shown to be predicted correctly for the relatively simple  $k-\epsilon$  model (Speziale, 1993).

## 2.5 Rotating Spanwise Channel Flow

The schematic for this case is shown in Figure 5. A fully developed flow between two infinitely wide and deep plates is rotated around an axis perpendicular to the plane of the flow. The predictions for this case are compared to DNS by Kristoffersen and Andersson (1993). The DNS has a turbulent Reynolds number

$Re_t = u_\tau h / \nu$  of 194. Here  $h$  is the channel half width and  $u_\tau = \sqrt{\nu \frac{d\bar{v}}{dy}}_{wall}$  is the turbulent velocity scale.

The pressure gradient is equal to 1. The Rossby number  $Ro$  for this case is defined as  $2h|\Omega|/U_b$ , where  $U_b$  is the bulk mean velocity of the flow in the channel.

The primary issue in modeling the equations for turbulent potentials for the case of channel flow was to get the correct wall asymptotics. In the equation for  $\phi$ , if  $C_{p2}^s$  and  $C_{p2}^w$  tend to some arbitrary constant other than 2.0 near the wall, then the terms involving the strain vector and the intrinsic vorticity vector vary like  $O(y^3)$  near the wall while the other terms vary like  $O(y^5)$  close to the wall. This leads to difficulty in integrating the equation up to the wall. In order to avoid this we make  $C_{p2}^s$  and  $C_{p2}^w$  tend to 2.0 near the

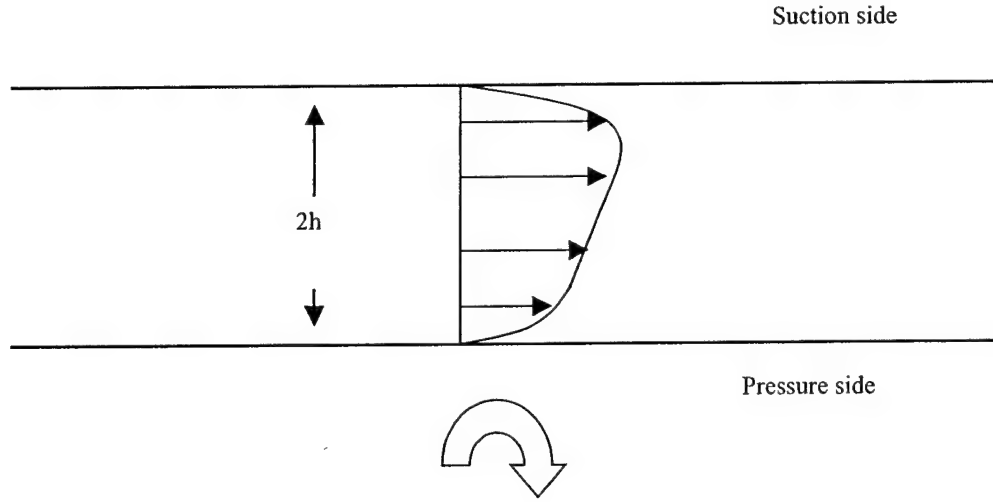


Figure 5. Fully developed spanwise rotating channel flow. The Block arrow denotes the direction of positive rotation. The axis of rotation is at a very large distance compared to the channel width.

wall in such a way such that an extra factor of  $(1 - \alpha)$  now multiplies the terms involving the intrinsic vorticity vector and the strain vector. Since  $(1 - \alpha)$  varies near the wall as  $O(y^2)$ , therefore the wall asymptotics of the  $\phi$  equation is correct, and we can integrate the equation up to the wall.

From Figure 6 we can see that for zero rotation, the mean velocity field is well predicted. Figure 7 shows that the shape of the velocity profile becomes asymmetric for  $Ro = 0.15$ , though the slope of the velocity profile predicted on the pressure side is not correct. Figure 8 shows that the slope is predicted correctly for a higher rotation rate of  $Ro = 0.5$ . Therefore we can say that the turbulent potential model is sensitive to spanwise rotation of a fully developed channel, and gives a good prediction of the velocity profile

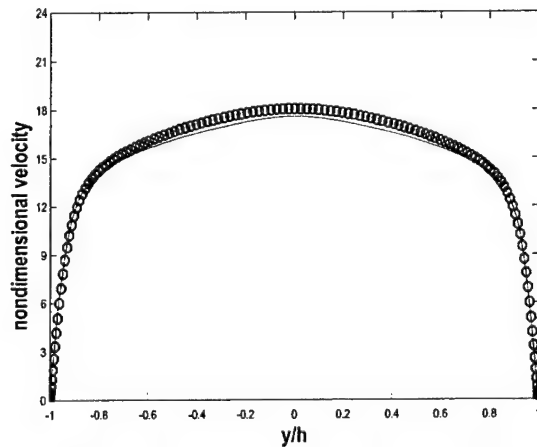


Figure 6. Mean velocity profile for  $Re_\tau = 194$ . No rotation is present. Mean velocity has been nondimensionalized with respect to  $u_\tau$ . Symbols denote DNS data while line denotes model prediction.

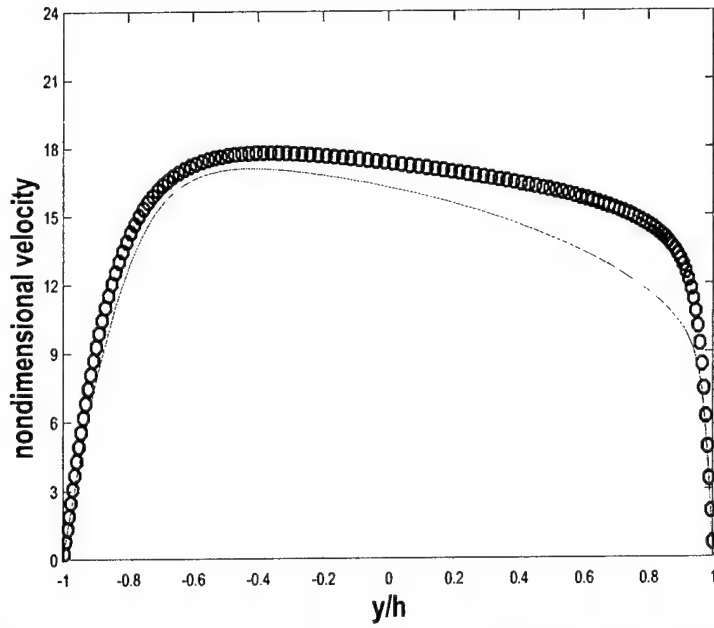


Figure 7. Mean velocity profile for  $Ro = 0.15$ . Symbols denote DNS data while line denotes model prediction.

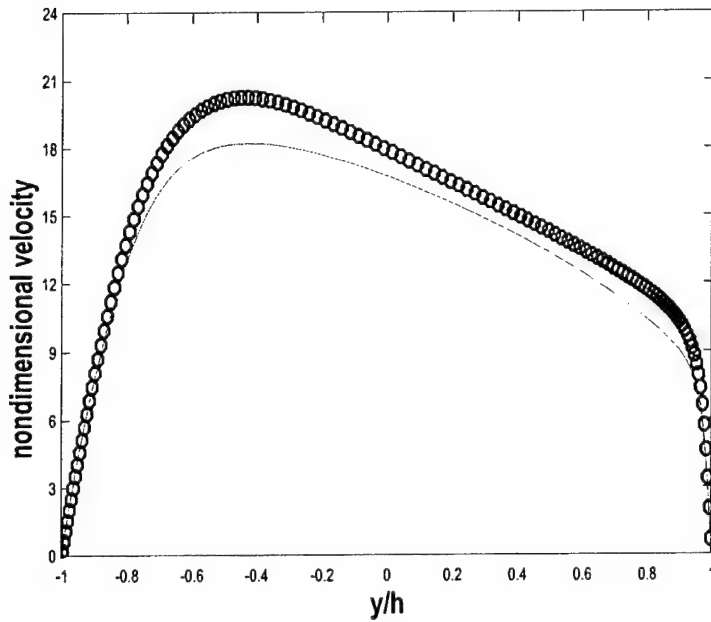


Figure 8. Mean velocity profile for  $Ro = 0.5$ . Symbols denote DNS data while line denotes model prediction.

## 2.6 Isolated turbulent trailing vortex

A turbulent trailing vortex is created by the wingtip of a plane. Since the trailing vortex is a case for which few experimental or numerical results are present, therefore we make some assumptions about the vortex which are the same as those made by Wallin and Girimaji (2000). Cylindrical coordinates are used to represent the components of the velocity field. Initially both mean axial and azimuthal velocities are present in the vortex. After some time, assuming that the axial velocity diffuses due to the turbulence, only the azimuthal velocity will be present. Consequentially the flow is homogenous in the  $z$  direction. The mean azimuthal velocity (i.e.  $\bar{v}_\theta$ ) gets affected only by the component  $\Psi_1$ . In order that the vortex grows at the right rate,  $\Psi_1$  should have the correct magnitude and radial profile.

A major difference between this case and the previous cases is that the turbulence is inhomogeneous in 2 directions, and therefore there is no one-to-one correspondence between the turbulent potentials and selected components of Reynolds stresses. Therefore, this is the first case where we will numerically solve (2.8) and find out the component of the strain vector  $s_1$ . Since this is not a wall bound flow therefore we cannot take (2.9) as a boundary condition. However, we can assume that at very large radius the turbulent quantities are inhomogeneous only in the  $r$  direction, i.e. the cylindrical and Cartesian coordinates start becoming similar at large radius. We can also assume close to isotropic conditions at large radius. Therefore we can take our boundary conditions as

$$\begin{aligned} s_1|_{r=R} &= 2S_{23} \\ \phi|_{r=R} &= R_{22} = \frac{2}{3}k \\ \text{or } \phi s_1|_{r=R} &= \frac{4}{3}kS_{23} \end{aligned} \quad (2.11)$$

Along with (2.11) we take zero-derivative boundary conditions for the turbulent potentials. The results for this problem are presented in terms of the circulation  $\Gamma = 2\pi r \bar{v}_\theta$ . Potential flow is present at points far away from the vortex core because of the absence of any significant stresses. Therefore, the circulation will be a constant  $\Gamma_0$  at the boundary. Hence, we take the zero-derivative boundary condition for the circulation as well. LIDAR (Coherent Doppler Laser Radar) measurements (Campbell et al., 1996) of an aircraft trailing vortex at Memphis airport have been taken for initial conditions and for comparing the final conditions with the results predicted by the model. The initial conditions that have been assumed for the turbulent quantities are taken according to the suggested values given by Wallin and Girimaji (2000). All the initial conditions are nondimensionalized with respect to  $\Gamma_0 = 350 \text{ m}^2/\text{s}$  and a critical radius  $R_c = 1.8 \text{ m}$ . They are  $k_0 = 10^{-5}$  and  $\varepsilon_0 = 10^{-8}$ . We also assume  $\phi_0 = 0.66k_0$  and  $\Psi_1 = 0$  because of initially isotropic conditions. Turbulent Reynolds number  $Re_\tau = 20 \times 10^6$ . The LIDAR measurement for the final circulation profile has been taken at a time  $t = 55 \text{ s}$  (which is equivalent to about 6000 non-dimensional time steps). The final result for this case can be seen in Figure 9. The circulation is falling at around  $\log(r) \approx 0.3$ , as apparent in the experiment. However, the rate of decrease is much slower than the measured values. Also, there seems to be an overshoot of the circulation, which is physically possible (Govindaraju and Saffman, 1971), it is not true for the experimental results. The circulation at around  $\log(r) = 0.1$  seems to have increased instead of decreasing.

Thus the results for the turbulent trailing vortex are not highly satisfactory, as the growth rate of the vortex seems to be very low. However, the model prediction does have the feature of having an unchanged core region. This is significantly better than the  $k$ - $\varepsilon$  model which gives a rapid expansion of the core region (Wallin and Girimaji, 2000).

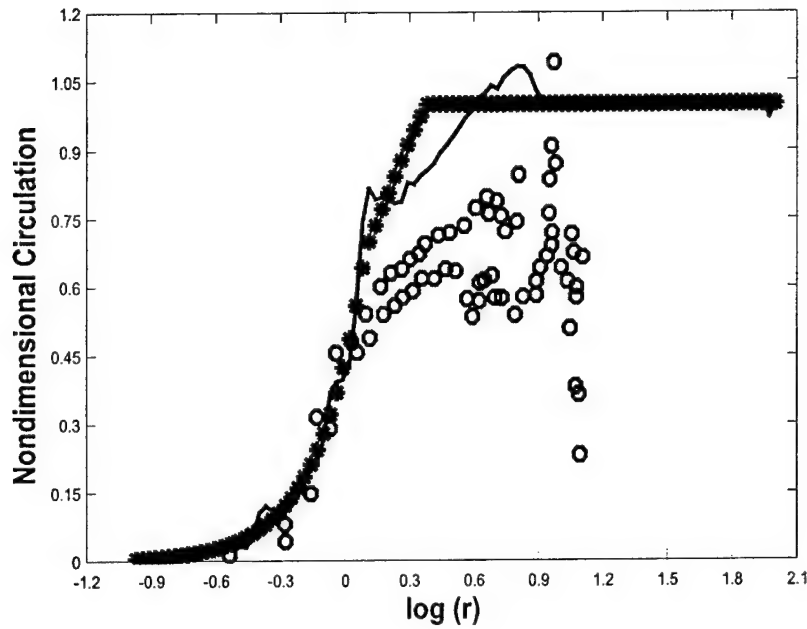


Figure 9. Circulation profiles of a trailing vortex. Symbol \* indicates initial circulation profile for both model and LIDAR measurement. Solid line gives final circulation profile predicted by model at  $t=55$  s. Symbol o indicates final circulation profile measured by LIDAR

## 2.7 Swirling Pipe Flow

The swirling pipe flow is the most difficult case to model because the one-to-one relationship between the Reynolds stress and the turbulence potentials is lost. Figure 10 shows the schematic diagram for this case. The  $z$ ,  $r$ ,  $\theta$  directions correspond to 1, 2 and 3 directions respectively.

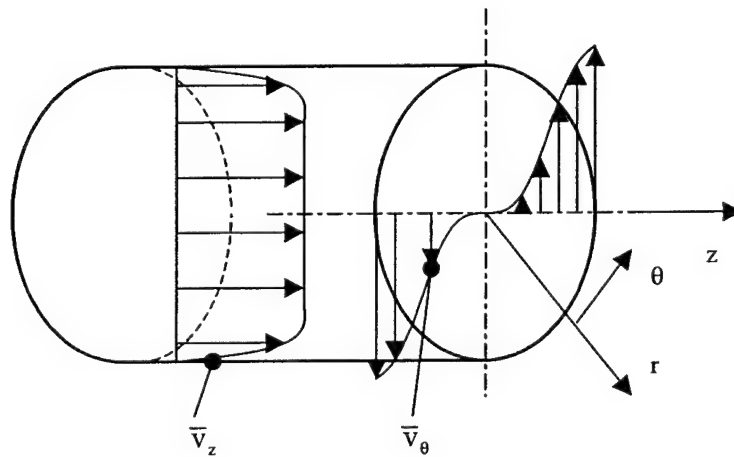


Figure 10. Schematic of swirling pipe flow. The velocity field is shown relative to a stationary frame of reference.

The model has been compared to the experiment by Imao and Itoh (1996). The calculations have been done with respect to a non-rotating frame, so that Coriolis terms are not present in the calculations. The radius of the pipe is  $R$ . The turbulent Reynolds number  $u_\tau R/\nu$  for this case is 572. The rotation rate is defined as  $\bar{v}_\theta|_{\text{wall}}/\bar{v}_z|_{\text{mean}}$ , and the three rotation rates tried out are 0, 0.5 and 1.0. The non-dimensional pressure gradients applied for the three cases are 1.0, 0.8 and 0.6 respectively.

The extra term which contributes to the model for this case is the vector  $\mathbf{A}$ , defined in (1.14). This term does not contribute to the channel flow or 2-D flows. This is because the term consists of vectors like  $\mathbf{s} \times \boldsymbol{\Psi}$  and  $(\hat{\boldsymbol{\omega}} - \mathbf{s}) \times \boldsymbol{\Psi}$  which is zero if the vectors  $\hat{\boldsymbol{\omega}}$  and  $\mathbf{s}$  are parallel to  $\boldsymbol{\Psi}$ . However, for a 3D flow this term can affect all the components of  $\boldsymbol{\Psi}$ .

Figure 11 compares the axial and azimuthal velocity profiles for  $N$  equal to 0., 0.5 and 1.0 respectively. Although the agreement of the model predictions with the experimental data is not very good, it does follow the trends shown by the data. As we go to higher rotation rates, the centerline axial velocity increases. Also, as rotation rate increases, the deficit between the azimuthal velocity profile predicted by the model and the laminar (and linear) azimuthal velocity profile increases. The overshoot of the azimuthal velocity profile near the wall decreases as the rotation rate is increased.

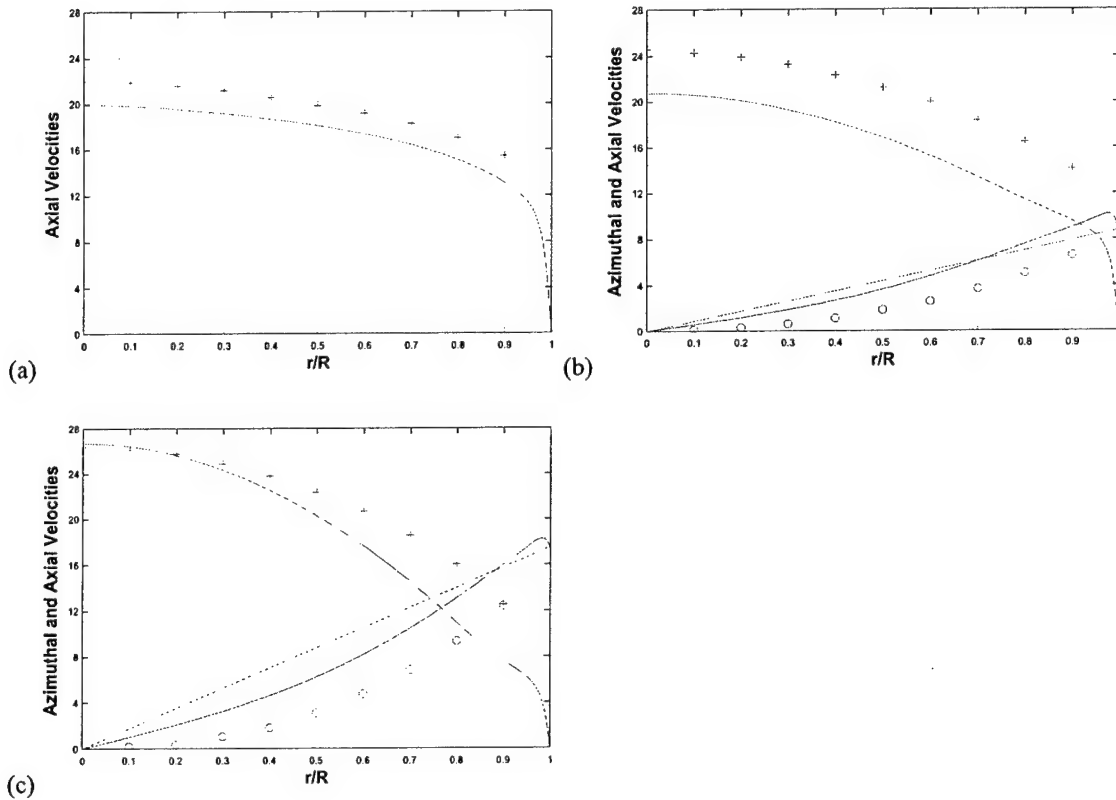


Figure 11. (a) Axial velocity profile for  $N=0$ , (b)  $N=0.5$ , (c)  $N=1.0$ . (b) Axial and azimuthal velocity profiles for  $N = 0.5$ . (c) Axial and azimuthal velocity profiles for  $N = 1.0$ . Symbols + indicate experimental results for axial velocity. Symbols o indicate experimental results for azimuthal velocity. Bold lines indicate model predictions. Dashed lines depict azimuthal velocity profile for laminar flow.

## 2.8 Streamwise rotating channel flow

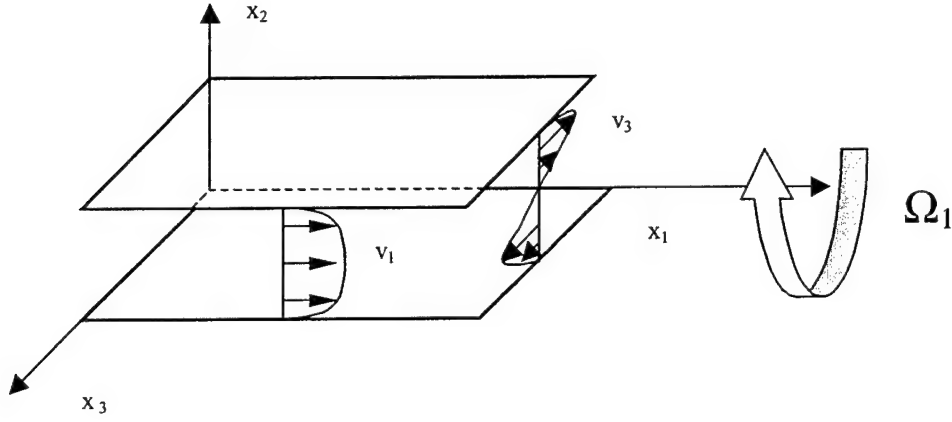


Figure 12. Schematic of the streamwise rotating channel flow

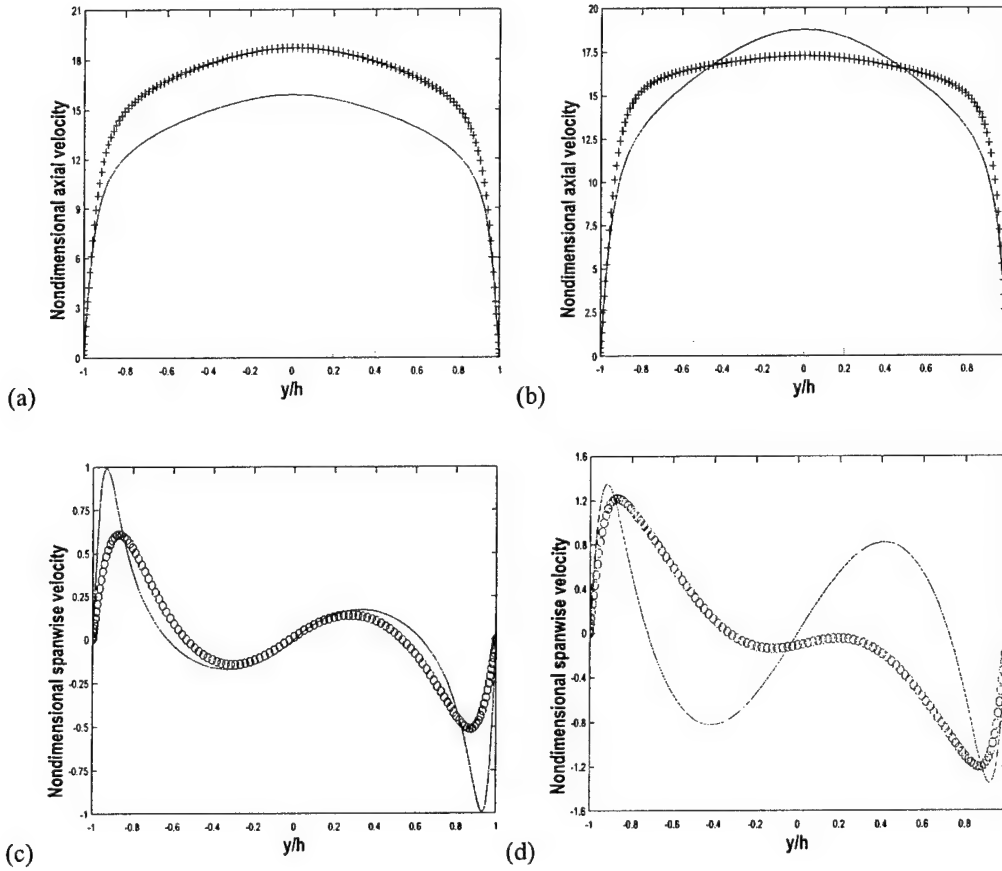


Figure 13. (a) Axial mean velocity at  $Ro = 3$ . (b) Axial mean velocity at  $Ro = 10$ . (c) Spanwise mean velocity at  $Ro = 3$ . (d) Spanwise mean velocity at  $Ro = 10$ . Symbols denote DNS. Line denotes model prediction.



The streamwise rotating channel flow consists of fully developed flow between two channels in the  $x_1$  direction which is then rotated around an axis along the  $x_1$  direction. As shown in Figure 12 both axial and spanwise velocities get generated in this flow. There is only one direction of inhomogeneity (i.e.  $x_2$ ). Thus we have a one-to-one correspondence between some of the Reynolds stresses and the turbulent potentials. This case has been tried out along with the swirling pipe flow in order to correctly calibrate the vector  $\mathbf{A}$  in the equation for  $\Psi$ . The vector  $\mathbf{A}$  will appear in this case because the flow is 3D. The vector  $\mathbf{A}$  is not seen in the equation for turbulent shear stresses in RANS models, although a one-to-one correspondence exists between the vector  $\Psi$  and the shear stresses  $R_{12}$ ,  $R_{23}$ . This may be because the exact equations for the turbulent shear stresses involve terms containing factors like  $(R_{11} - R_{22})$  and  $(R_{33} - R_{22})$ , which cannot be represented by only  $\phi$  and  $k$ . The results of the model predictions have been compared to DNS by Oberlack, Cabot and Rogers (1998). The Reynolds number for the flow is given by  $Re_\tau = hu_\tau / \nu = 180$  where all the quantities have the same definition as for the case of spanwise rotating channel flow. The Rossby number is given by  $Ro = 2\Omega h / u_\tau$ . The DNS data is there for  $Ro=3.0$  and  $Ro=10.0$ , therefore these are the rotation rates against which the model is compared. From (a) Axial mean velocity at  $Ro = 3$ . and **Error! Reference source not found.** we can see that the streamwise velocity is predicted quite well by the model. For higher rotation rates the model seems to be having a tendency to give a more parabolic profile at the center, whereas the DNS seems to be giving a flatter profile. From Figure 13 we see that the spanwise velocity is predicted well for low rotation rates, but deviates appreciably from the DNS at high rotation rates.

## 2.9 Conclusions

- The model correctly predicts that the dissipation rate decreases with an increase in rotation rate.
- The model is frame consistent with frame invariant flow-dependent vectors mathematically defined. The frame rotation rate appears in the equations only through the intrinsic vorticity vector.
- The model gives the wrong evolution rate for the turbulent kinetic energy for initially isotropic turbulence subjected to plane shear.
- 2D rotating channel flow has been well predicted.
- Model predictions do not give the required growth rate for the trailing vortex. However, the results are better than the  $k-\epsilon$  model.
- A vector  $\mathbf{A}$  is present in the model which is constructed in such a way that it contributes only for 3D flows. Both swirling pipe flow and streamwise rotating channel flow have been predicted reasonably well.

The turbulent potential model has been constructed in such a way that it is sensitive to frame rotation as well as streamline curvature. At the same time, it is also frame consistent. In order to construct a frame consistent model, we first identified the form of the transport equation for the turbulent potentials, and then constructed frame invariant flow dependent vectors (i.e. the strain and intrinsic vorticity vectors). Thus we ensure that any dependence of the model on the frame rotation rate has to be through the intrinsic vorticity vector. The similarity of the model with RANS models for flows with only one direction of inhomogeneity is then used in order to find out the form of the various budget terms in the model (i.e. pressure strain, dissipation, turbulent transport etc.). This model is then extended for 3D flows, and an extra term has to be added which contributes to only 3D flows.

The results show that the model does a good job of predicting the flows in the axial direction for swirling/streamwise rotating flows. The model also predicts correctly the streamwise velocity profile for the spanwise rotating channel flow. The spanwise/azimuthal velocity is not well predicted for either swirling flows or the trailing vortex flow, however the spanwise/azimuthal velocities are much smaller than the axial velocity and therefore it is not as important as the axial velocity. The wrong evolution rate for the non-rotating homogenous shear flow is of some concern.

Predicting rotating turbulent flows is a very difficult task. The corrections to the model to account for rotation are not as elegant as initially desired. Nevertheless, a great deal was learned in this project concerning rotating turbulent flows, their physics, and how to correctly model rotation.

### **3. Transition**

#### **3.1 Introduction**

Transition to turbulence is a stochastic process which is only partially understood. Depending to a large extent on the characteristics of the initial disturbances a laminar boundary layer flow will experience different transition processes until it finally develops into fully developed turbulence. Typically, two types of transition scenarios are considered - natural transition and bypass transition.

If the magnitude of the disturbance is small enough, the excited instabilities will grow like typical linear theories predict. Once the instabilities are large enough, spanwise fluctuations will be triggered and then develop to the same scale as the streamwise fluctuation waves. Subsequently, non-linear effects take over and transition will take a route of exponential growth of instability waves, which is known as "secondary instability" and is a result of the interaction between the inertial scale disturbances and local heterogeneities. Following this stage, the process is rather a breakdown than a growth. Instabilities ultimately burst forth into patches of irregular motion which are termed turbulence spots (Emmons, 1951). These intermittent spots are interspersed by laminar flow but they develop rapidly and eventually coalesce into fully turbulent flow. A transition process evolving through the stages described above is termed "natural transition".

Alternatively, in some circumstances, the disturbances can be at the inertial scale initially and the non-linear effects immediately come in to play. The linear growth process is bypassed and secondary instability and turbulence spot occurs very quickly and the flow becomes turbulent in a short distance. Obviously, such a transition mechanism is quite different from natural transition. It is termed "bypass transition" and is stochastic in nature. In addition to the difference in stages experienced by the flow, the characteristics of the flow patterns in their common stages can be different. For example, for a transitional boundary flow, the turbulent spots in the bypass transition are generated by free-stream eddies while the classical Emmons type spots in the natural transition are usually stimulated by instabilities near the wall (Jacobs & Durbin, 2001).

Due to the existence of apparently different transition mechanisms, the attempts to develop a universal methodology to model transition to turbulence are often met with skepticism. Nevertheless, for most engineering applications, we only require the model to produce an accurate prediction of the mean flow behavior in the transition region. This allows us to neglect the mechanism of instability evolution in the transition and only take care of quantities that contribute significantly to the mean flow variables. There is no doubt that we can always find some general traits of flows in the transitional zone, which distinguish them from either laminar or full turbulent flows. Basically, the transitional zone is a region for the fluctuations of flow variables to develop from small scales into the full span of turbulent scales. These intensities of the fluctuating quantities are large enough to measure the "random" behavior of the flow and they are small enough to keep the stochastic part from affecting the mean flow significantly until the very end of the transition. The methodology of this work recognizes the fact that the contribution to the mean flow of the small amplitude fluctuations in transitioning flow can be taken into account by certain terms in the turbulence model.

#### **3.2 Review of Transition Prediction Approaches**

Predicting the onset of turbulent flow is a critical component of many engineering and environmental flows. The characteristics of laminar and turbulent boundary layers are so different that the precise location of this relatively abrupt transition can have a profound influence on the overall drag, heat transfer, and performance properties of devices that operate in the transitional regime. The prediction of boundary layer

transition is complicated by the fact that it does not correspond very directly to the onset of instability. Stability analysis for boundary layers is well developed and very predictive of the behavior of small disturbances, however the instabilities go through a series of complex non-linear and three-dimensional processes before turbulence itself actually develops. In addition, stability analysis is less helpful with the prediction of by-pass transition where external free-stream disturbances by-pass the classic instability mechanisms and initiate the non-linear three-dimensional transition process directly.

Traditional methods for predicting transition rely on correlations. For example, van Driest & Blumer (1963) suggest the implicit correlation:

$$1690 \text{Re}_{x,tr}^{-1/2} = 0.312(m + 0.11)^{-0.528} + 4.8\delta_{99}^2 \text{Re}_{x,tr}^{1/2} T^2 \quad (3.1)$$

where  $\text{Re}_{x,tr}$  is the transition Reynolds number based on the local free-stream velocity  $U$ , the parameter  $m$  is related to the dimensionless pressure gradient ( $m=0$  for zero pressure-gradient),  $\delta_{99}$  is the local 99% boundary layer thickness, and  $T = \sqrt{\frac{2}{3}} k / U$  is the local free-stream turbulence intensity. This is only one of many proposed correlations. While they appear relatively simple, they are actually quite awkward to implement in a general purpose CFD code. In a general code, correlations require each point on the boundary to determine non-local quantities, such as free-stream values, distance downstream from the leading edge and boundary layer thickness. Unambiguous definitions for such quantities in a general situation are very difficult to formulate. Many CFD codes simply resort to requiring the user to specify the transition location. Once the transition location has been determined, there is the further difficulty of determining how the turbulence model should be prompted to become active. Solutions to this problem range from specifying large turbulent kinetic energy at the wall where transition is expected to occur to specifying local large source terms in the turbulence evolution equations (artificial production). None of these methods of ‘tripping’ the turbulence model are particularly reflective of the actual physical transition process, and add further ambiguity to the already uncertain transition location. In addition, ‘tripping’ of this sort is largely code dependent, so that the same theoretical model can produce different results in different codes, or even within the same code using different meshes.

An alternative approach is to use the turbulence model itself to predict the transition location. This is a very natural approach in by-pass transition, since the model is effectively *on* in the free-stream anyway to predict the free-stream turbulence. A number of studies on boundary layer by-pass transition prediction using low Reynolds number  $k/\epsilon$  models have been performed, and Savill (1990 & 1996) are good reviews of how various flavors of the  $k/\epsilon$  models perform. The overall conclusion is that none performs well for all the flows considered. More recent work using a  $k/\epsilon$  intermittency model (Suzen & Huang, 2001) has shown more success. However, none of these models attempts to predict natural transition or relaminarization.

### 3.3 Motivation

While the idea of using RANS models to predict transition may have originally been motivated by practical considerations such as ease of implementation, it also has a solid theoretical justification that has not been discussed previously. The derivation of the Reynolds Averaged Navier-Stokes (RANS) and accompanying Reynolds Stress Transport (RST) equations are simply a mathematical reformulation of the governing Navier-Stokes equations. There are no physical assumptions or restrictions on the range of applicability of these equations, as presented below.

$$\frac{\partial \mathbf{u}}{\partial t} + \nabla \cdot (\mathbf{u}\mathbf{u}) = -\nabla p + \nabla \cdot \nu \nabla \mathbf{u} - \nabla \cdot \mathbf{R} \quad (3.2a)$$

turbulent transport, and dissipation are only expected to influence the very last stages of transition (the overshoot recovery) and should have little affect on the critical transition location. Most models for the rapid pressure strain usually only capture rapid shear correctly because this is the important case for boundary layer and free-shear flows. Reynolds and Kassinos (1995) have a modeling framework that can capture any rapidly distorting flow.

Due to the complexity of solving the Reynolds stress transport equations, two-equation models such as  $k/\varepsilon$  are very popular. The  $k$ -equation is derived by taking one half of the trace of Eqn 3.2.

$$\frac{\partial K}{\partial t} + \mathbf{u} \cdot \nabla K = -\frac{1}{2} \overline{u'_j u'_k} \frac{\partial u_j}{\partial x_k} - \frac{\partial}{\partial x_k} \left\{ \overline{u'_j \left( \frac{1}{2} u'_i u'_i + \frac{p'}{\rho} \right)} \right\} - \nu \overline{\left( \frac{\partial u'_i}{\partial x_j} \right)^2} + \nu \nabla^2 K \quad (3.4)$$

Two very important changes take place when only the  $k$ -equation is solved. First, pressure strain disappears entirely. This is because this term only redistributes energy between various Reynolds stress components, it does not influence the overall energy content. Unlike spatial redistribution (transport terms) this intercomponent redistribution is important, particularly in the boundary layer. It takes energy out of the amplified streamwise fluctuations and transfers it to the normal and spanwise fluctuations, damping the streamwise fluctuation growth and feeding the normal and spanwise velocity fluctuations. Two equation models (like  $k/\varepsilon$ ) are fundamentally incapable of capturing physical processes that involve intercomponent energy redistribution. In addition, the production term is no longer exact. The Reynolds stress tensor in this term must now be modeled. The classic Boussinesq eddy viscosity model is

$$\mathbf{R} = \frac{2}{3} K \mathbf{I} - \nu_T (\nabla \mathbf{u} + \nabla \mathbf{u}^T) \quad (3.5)$$

Where the eddy viscosity is given by  $\nu_T = \frac{C_\mu K^2}{\varepsilon}$ . More complicated versions of this equation are

possible and are referred to as nonlinear eddy viscosity models or algebraic Reynolds stress models. They all have the same fundamental problem for predicting transition. These models assume that the fluctuations are somehow in equilibrium with the mean flow. They suppose that a given shear level results in a given turbulence level. The transition process is as far from an equilibrium situation as possible. During transition, fluctuation amplitudes grow exponentially in time (moving with the fluid), while shear levels remain almost constant.

Despite these difficulties, it is interesting to note that two-equation models still can produce qualitatively transition-like behavior, with a rapid increase in turbulence levels and skin friction from low initial levels. This suggests that these differential equations, and by inference the modeled RST equations, have the mathematical capability of produce exponentially growing solutions, and transitional behavior. With the added accuracy in the production and rapid pressure-strain terms, it is expected that RST models could potentially constitute a very accurate transition prediction methodology. However, classic RST models represent a significant investment in programming complexity and computational resources. The turbulent potential model used in this work (Perot, 1999) (Perot & Wang, 1999) (Zhang & Perot, 2000) represents an effective compromise. It is a reformulation of the RST equations that retains the non-equilibrium and energy redistribution physics, but which can be implemented at a computational cost and programming complexity comparable to the very popular two equation models. The turbulent potential model's formulation and success in predicting fully turbulent flows has been discussed in prior publications (Perot & Taupier, 1999) (Tsuei & Perot, 2000) (Are, Zhang & Perot, 2001). In this work we focus on its unique abilities to predict transition in boundary layer flows. We will demonstrate the ability to predict by-pass transition, the affects of pressure gradients, natural transition, relaminarization, and the affect of noise levels on natural transition.

### 3.4 Flat plate boundary layer in zero pressure gradient

The process of transition is studied by looking at the evolution of the friction coefficient along the streamwise direction. The friction coefficient is a very sensitive indicator of transition that increases dramatically as transition occurs. The model predictions are compared to experimental data with different turbulence intensities. The mean velocity is initially uniform flow for all cases and the initial values of velocity  $U_0$ , turbulence Reynolds number  $Re_T = k^2/(\nu\epsilon)$ , turbulence intensity level

$Tu = \left(\frac{2}{3}k\right)^{1/2}/U_\infty$  for five experimental cases with different turbulence intensities are given in Table

3.1. The initial values of the turbulent kinetic energy  $k$  are determined using  $k = 3/2(Tu \cdot U_0)^2$ . For the  $Tu = 0.03\%$ ,  $Tu = 1.25\%$  and  $Tu = 1.3\%$  cases, the initial turbulent dissipation rate  $\epsilon$  is calculated from  $Re_T$  using  $\epsilon = k^2/(\nu Re_T)$  and the value of  $Re_T$  is assumed. Results are not very sensitive to reasonable values of  $Re_T$ . For the  $Tu = 3\%$  (T3A) and  $Tu = 6\%$  (T3B) cases, the data for  $k$  is available, and the initial values of  $\epsilon$  are determined from  $\epsilon = -U_\infty \frac{dk_\infty}{dx}$ , where the subscript " $\infty$ " represents parameters in the free stream. The values of  $Re_T$  for these two cases listed in Table 3.1 are just calculated from  $\epsilon$ . The initial potentials  $\phi$  and  $\psi$  are set as  $2/3k$  and zero respectively. All experiments were performed in air so  $\nu = 1.55 \times 10^{-5}$  was used in every case.

$U_0$ (m/s)	$Re_T$	$Tu$	Source
24.4	100	0.03%	Schubauer & Klebanoff
22	250	1.25%	Abu-Ghannam & Shaw
14.42	250	1.3%	Dhawan & Narasimha
5.4	200	3.0%	ERCFTAC, T3A
9.4	200	6.0%	ERCFTAC, T3B

Table 3.1 Initial flow parameters at the leading edge of a zero pressure gradient boundary layer

The friction coefficient is plotted against,  $Re_x$ , the Reynolds number based on downstream position, in Figure 14. The friction coefficient correlations for laminar and turbulence flows,  $C_f = 0.664 Re_x^{-1/2}$  and  $C_f = 0.027 Re_x^{-1/7}$  respectively, are also plotted with dashed lines for comparison. Overall, the ability of the present model to predict the critical transition location is quite good. However, the natural transition case,  $Tu=0.03\%$ , shows some discrepancy with the experimental data of Schubauer (1955) at  $2.8 \times 10^6$ . Actually, this discrepancy is somewhat expected given the model initial conditions. Experiments of natural transition show a wide range of transition locations from a high value of  $Re_x = 5.0 \times 10^6$  measured by

Wells (1967) to classical predictive theories such as  $e^9$  rule which predict a value of  $2.0 \times 10^6$  (Warsi, 1999). This range of results is commonly attributed to different noise levels in the various experiments. We show later that the model can actually predict the entire range of natural transition experiments by varying the model initial conditions. We believe that the ability of this model to predict natural transition is a unique characteristic that is not demonstrated by other RANS models. For the highest inlet turbulence intensity case (T3B,  $Tu=6.0\%$ ), the level of friction coefficient turns out to be at high values in the pre-transitional region. A recent DNS study (Jacobs and Durbin, 2001) also reported a similar over prediction for a  $Tu=7.0\%$  case.

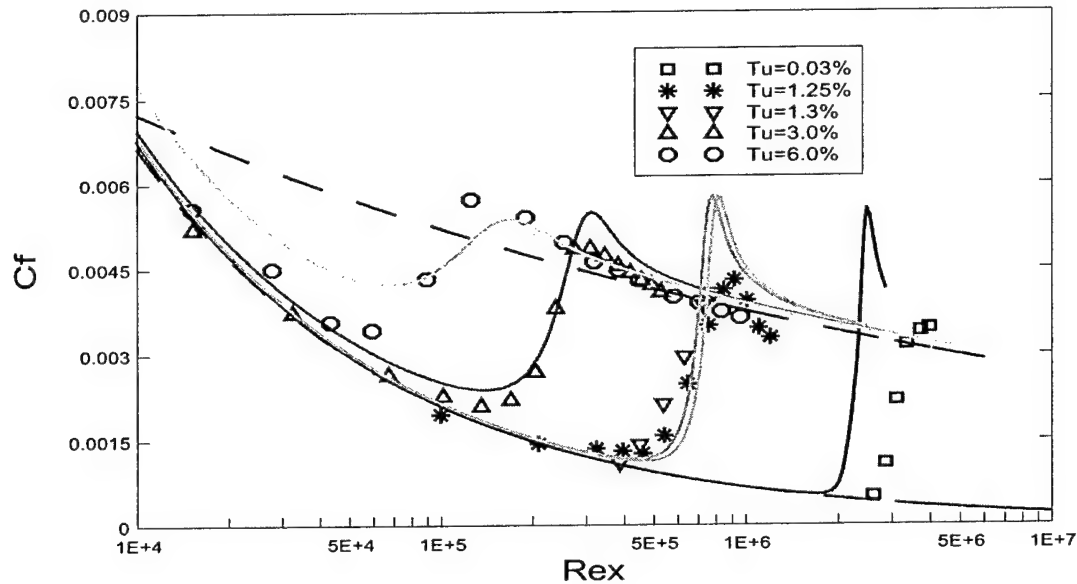


Figure 14. Transition in zero pressure gradient boundary layer at various initial turbulence intensities. The symbols represent experiment data and the lines are the present results. Dashed lines are fully laminar and fully turbulent correlations.

The other significant departure of the model predictions from the experiments is in the overshoot in the friction coefficient that occurs at the very end of the transition process and in the transition length. Predicting this overshoot and length correctly is not as important as predicting the transition location itself. Interestingly, the model does show the characteristic overshoot behavior found in experiments, but over predicts the extent of this overshoot. Our current hypothesis is that this discrepancy is largely caused by the use of boundary layer equations to solve for the velocity and turbulence variables, and is not due to the model itself. The boundary layer equations are based on the premise that streamwise second derivatives are small. During the later part of transition, as the flow suddenly becomes turbulent, the boundary layer grows quite dramatically, and the assumption of small streamwise second derivatives is not very accurate. Including these streamwise derivatives is expected to add considerable diffusion and significantly reduce the current excessive overshoot behavior. The fact that the overshoot error increases as the turbulence intensity decreases is consistent with this behavior, because the lower intensity transition events are also more abrupt and therefore violate the boundary layer approximations the most severely.

Two other numerical predictions, both performed by Suzen et. al. (2000), but using their  $k-\varepsilon$  intermittency model and another  $k-\varepsilon$  model (Launder & Sharma, 1974) respectively, are plotted in Figure 15 for the T3A case. The  $k-\varepsilon$  model predictions are not particularly good for this particular case. In contrast, Suzen's model captured the late stage of the transition region (including the overshoot) very well, but the transition onset was delayed. The present calculation, as shown in Figure 15, shows a

smoother transition behavior. In other words, the present model predicts not only a correct position of transition onset, but also a fairly accurate length of the transition region.

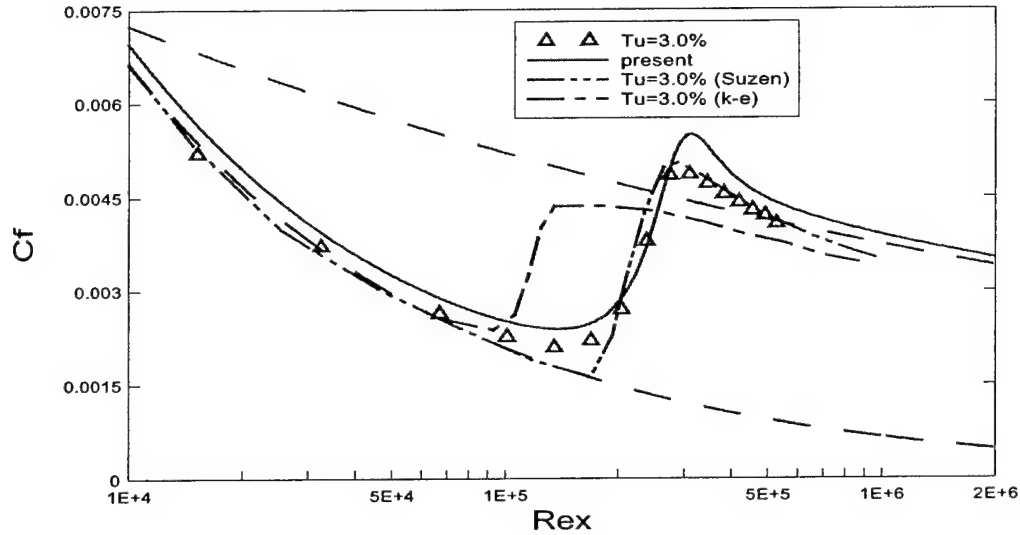


Figure 15. Comparison of predictions of transition in zero pressure gradient boundary layer for T3A case. Symbols represent experiment data and lines are the predictions.

The comparison of the Reynolds number based on momentum thickness,  $Re_\theta$ , and shape factor,  $H$ , with experiments and results from other numerical models are shown in Figure 16 and Figure 17 respectively for T3A case. It can be noted that the present prediction always stays between the other two simulations. The fact that Suzen's model has a slight later prediction of the onset of transition is also visible from the  $H$  curves. The streamwise mean velocity profiles calculated using the present model are compared at four downstream stations with the experimental T3A data and Suzen's predictions in Figure 18(a) through Figure 18(d). It is evident from these figures that the model predictions agree very well with the experimental data even for the detailed mean velocity profiles.

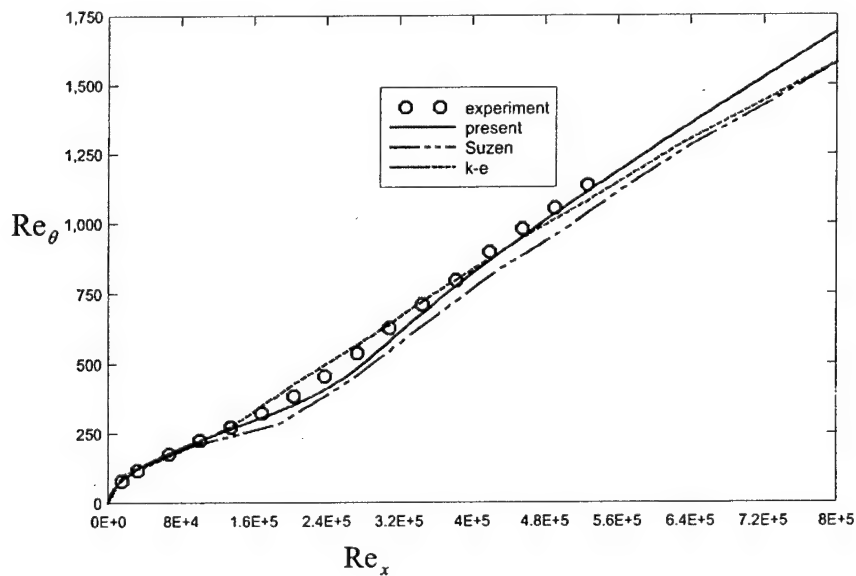


Figure. 16 Comparison of  $Re_\theta$  for T3A case.

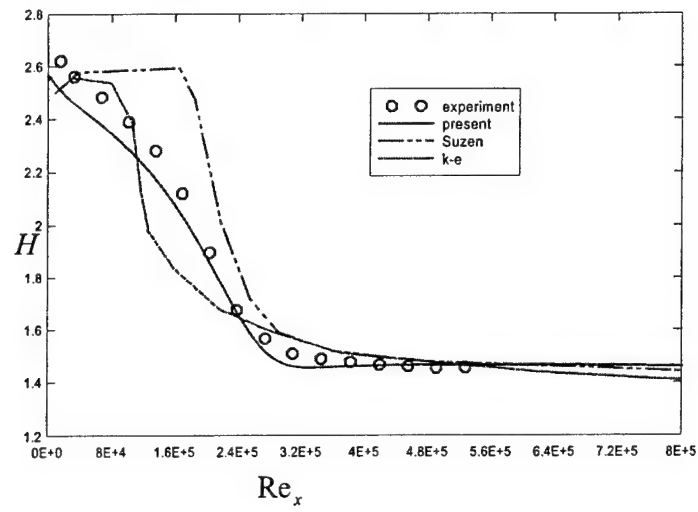




Figure 17. Comparison of H for T3A case.

### 3.5 Flat plate boundary layer in non-zero pressure gradient

Model predictions of transition in two variable pressure gradient boundary layers are compared with the experimental data of Coupland (1990) in Figure 19. The initial turbulence levels of these two cases are 3.0% (T3C3) and 6.6% (T3C1) respectively. For both of these flows, the pressure gradient is initially negative (favorable) and then positive (adverse) in a profile that was designed to roughly approximate the flow over a turbine blade. The pressure gradient profiles for the two different cases are roughly equivalent. The initial conditions are listed in Table 3.2 and are fully determined by the initial experimental data. It is very difficult to use correlations to predict this variable pressure gradient flow because the pressure gradient does not correspond closely to any single Falkner-Skan situation. In addition, the RANS models tested by Savill (1990) showed some difficulty with these cases.

The model predicts the transition location in these complex variable pressure-gradient boundary layers quite well. Note that in both cases the initially favorable pressure gradient has delayed transition compared to the flat plate case. The pressure gradient data is not provided beyond the range of the experimental data, so we can not continue the 3% case beyond the experimental data. Predictions given by Suzen et. al. (2000) are compared with the present calculation for T3C1 case again in Figure 20.

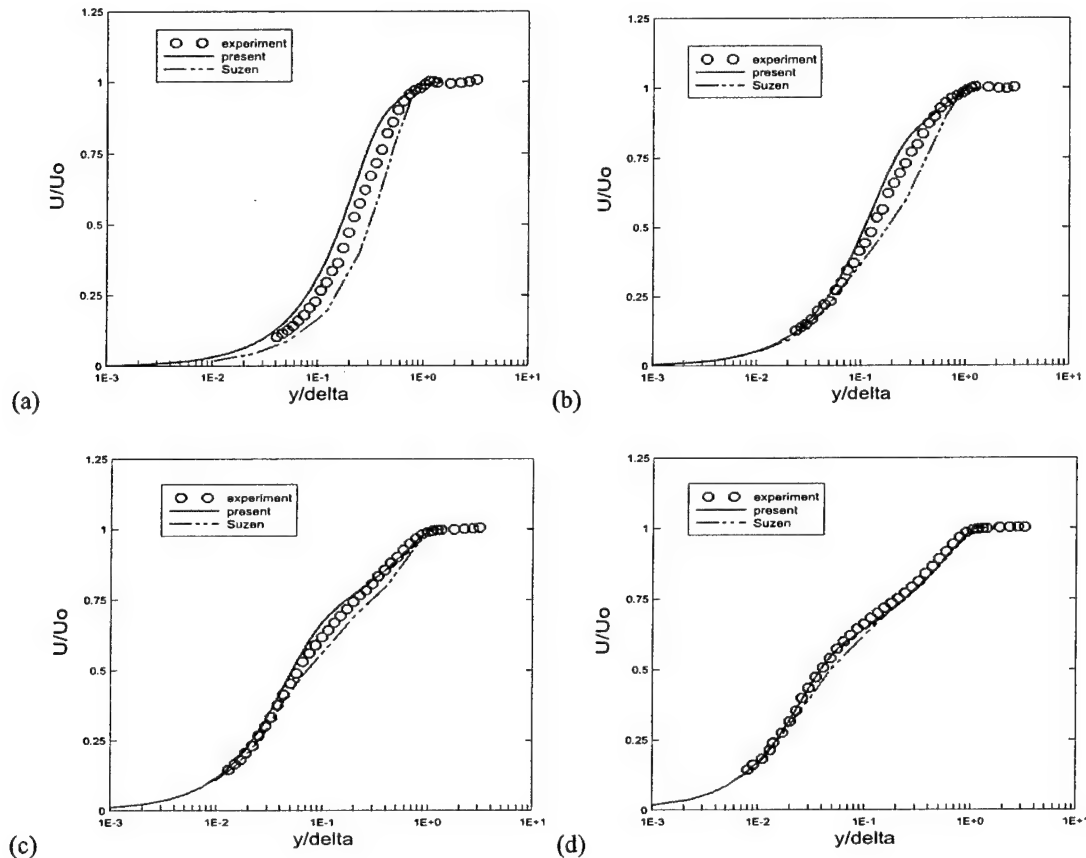


Figure 18. Mean streamwise velocity profiles for T3a case. (a)  $Re_x = 1.35 \times 10^5$ , (b)  $Re_x = 2.04 \times 10^5$ , (c)  $Re_x = 2.74 \times 10^5$ , (d)  $Re_x = 4.19 \times 10^5$ .

$U_0$ (m/s)	$Re_\tau$	$Tu$	Source
5.9	160	6.6%	ERCOFTAC, T3C1
3.7	100	3.0%	ERCOFTAC, T3C3

Table 3.2 Initial flow parameters at the leading edge of a variable pressure gradient flat plate boundary layer

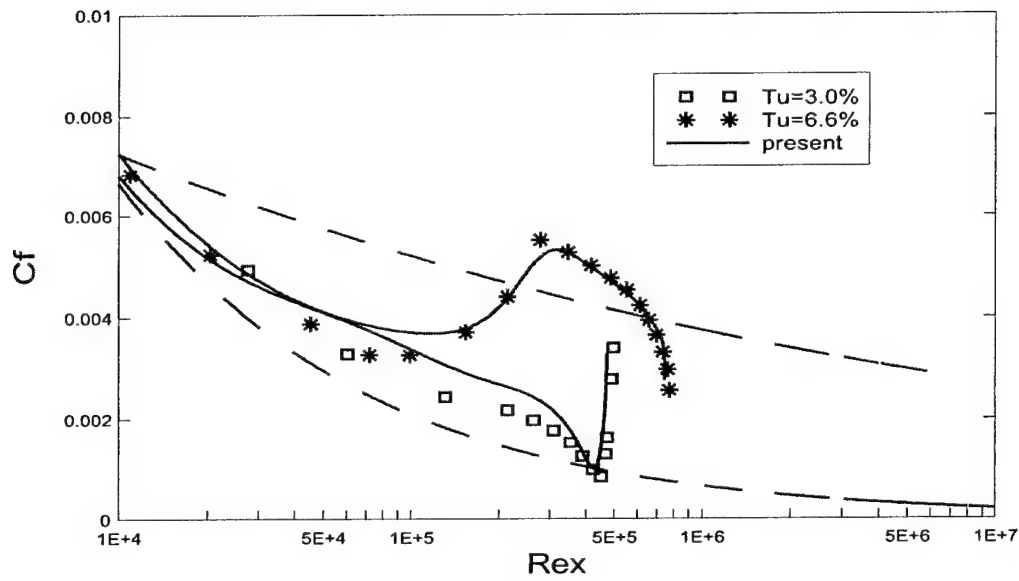


Figure 19. Transition in non-zero pressure gradient boundary layer at various initial turbulence intensities. The symbols represent experiment data and the lines are the present results.

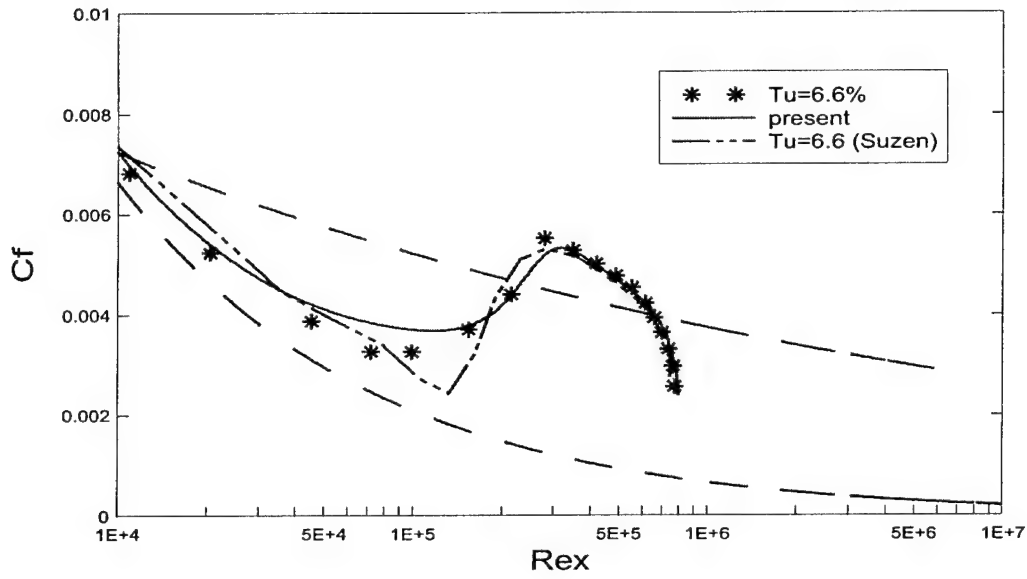


Figure 20. Comparison of predictions of transition in non-zero pressure gradient boundary layer for T3C1 case. Symbols represent experiment data and lines are the predictions.

Figure 21 shows the comparison of  $Re_\theta$  computed by the present model and the two other models with the experiment data for T3C1 case. Predictions of the shape factor profiles using the three models are plotted in Figure 22 along with the experimental data. Again, the present model exhibits excellent performance in calculating the shape factor in the transition region.

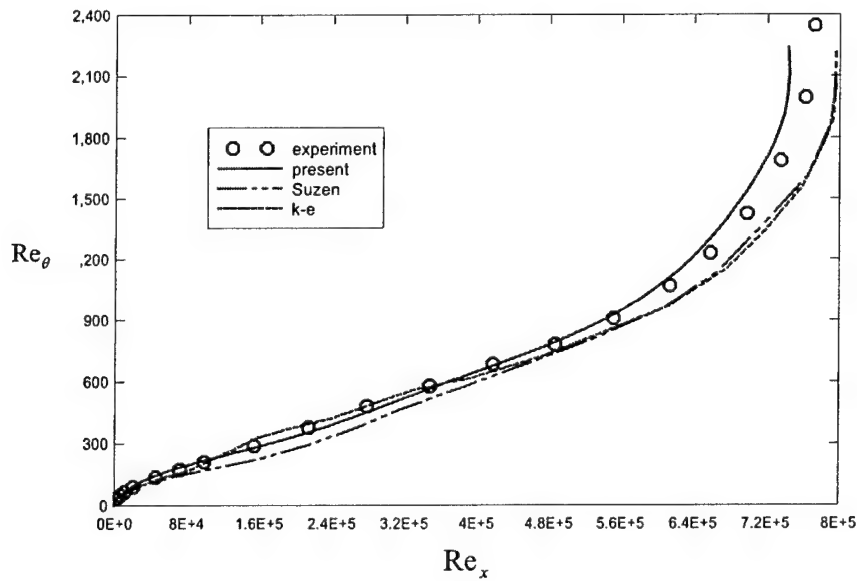


Figure 21. Comparison of  $Re_\theta$  for T3C1 case.

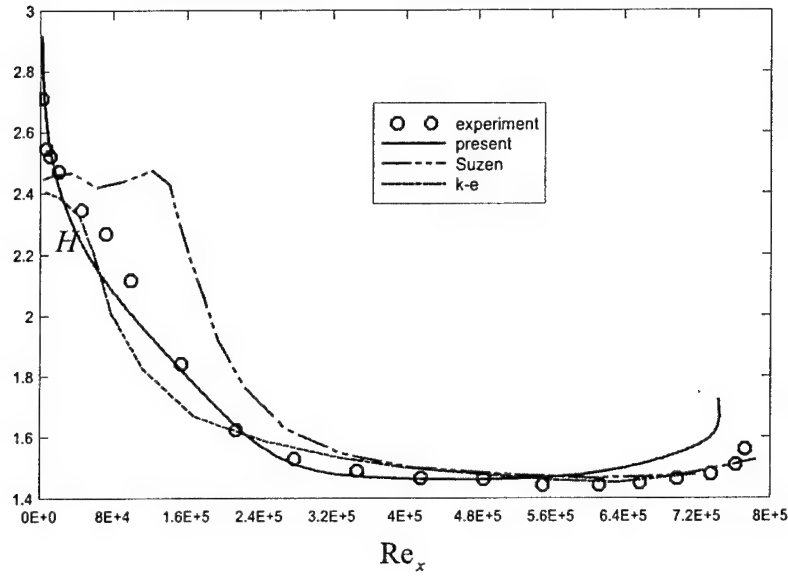


Figure 22. Comparison of  $H$  for T3C1 case.

### 3.6 Acoustic Effects on Natural Transition

It was mentioned previously that acoustic effects (wind tunnel noise) can have a fairly strong influence on natural transition. The experiment of Wells (1967) is commonly assumed to be largely free of acoustic noise, and therefore gives a high "quiet" transition location of  $Re_{x,tr} = 5.0 \times 10^6$ . Our initial prediction of  $Re_{x,tr} = 2.0 \times 10^6$  is close to the low (noisy) end of the experimental range. The experiments of Schubauer (1955) attempted to reduce noise levels, but were clearly not as successful in this respect as the later experiments of Wells.

Interestingly, the turbulent scalar potential represents irrotational fluctuations (see Perot 1999), and could be a very good measure of the average acoustic forcing. Our initial natural transition prediction (Fig. 2.1) was with relatively high noise levels of  $\phi = 2/3k$ , and is actually quite close to "noisy" experiments. If one reduces the initial scalar potential  $\phi$  to a value of  $0.12k$ , the onset of the transition will be delayed to  $5.0 \times 10^6$ , which agrees with Wells (1967). One can also match the data of Schubauer (1955)  $Re_{x,tr} = 2.8 \times 10^6$  in Table 2.1 by using  $\phi = 0.4k$ . All three simulations are shown in the  $C_f - Re_x$  curve plotted in Figure 23. This demonstrates the models ability to accurately capture the affects of noise on natural transition. The effects of noise on bypass transition are present but are less significant.

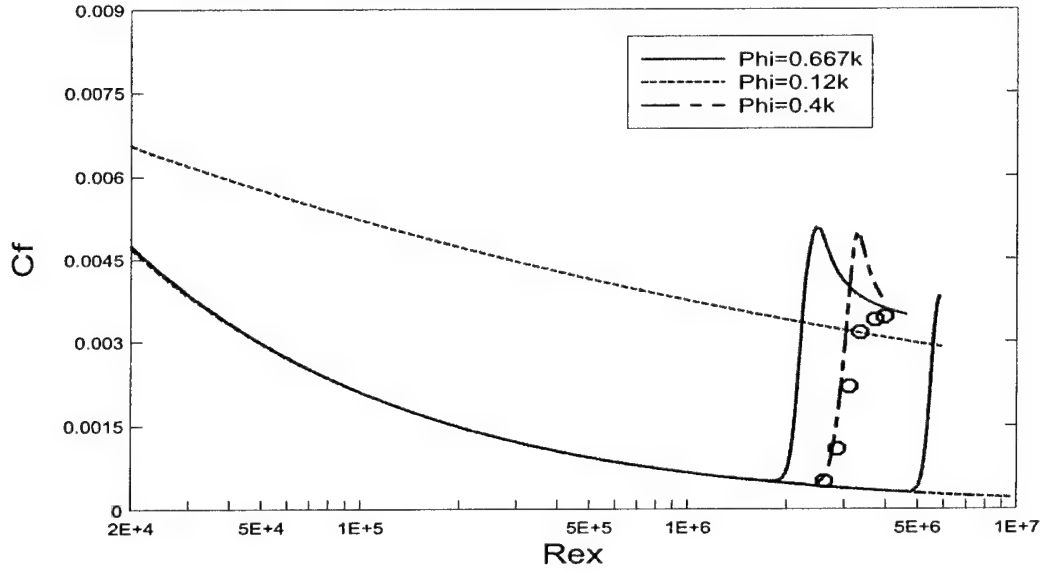


Figure 23. The acoustic effects on the natural transition at  $Tu = 0.03\%$ . Dashed lines are fully laminar and fully turbulent correlations.

### 3.7 Relaminarization in Turbulent Channel Flow

Almost as critical as transition, is the process of relaminarization, where a turbulent flow decays to a laminar state. Relaminarization can occur because of strong stratification, strong rotation, or in the case of channel flow, due to a reduction in the driving pressure gradient. Figure 24 shows predictions of the skin friction in channel flow for various bulk Reynolds numbers  $Re = \frac{\bar{u}_b h}{\nu}$ , where  $h$  is the channel half height

and  $\bar{u}_b$  is the average velocity. The figure also has dashed lines for the laminar exact result  $C_f = \frac{8}{3} Re^{-1}$  and the turbulent correlation of Dean (1978)  $C_f = 0.044 Re^{-0.227}$ . Here the skin friction coefficient is

calculated using  $C_f = \frac{\tau_w}{\frac{1}{2} \rho u_0^2}$ , where  $\tau_w$  is the wall shear stress and  $u_0$  is the center line velocity of the

channel. The model shows a clear relaminarization at  $Re_b = 1700$  ( $Re_\tau = 120$ ). Experiments and DNS (Keefe, 1992) indicate a transition Reynolds number of close to 1000 ( $Re_\tau = 60$ ). So the model could be improved. However, a theoretical study by Orszag (1971) showed the linear instability for a channel flow occurs at  $Re_b = 1600$  ( $Re_\tau = 110$ ). It is our observation, that this relaminarization location is strongly influenced by the low Reynolds number behavior of the model (particularly the dissipation and pressure strain term), and not the transition term itself.

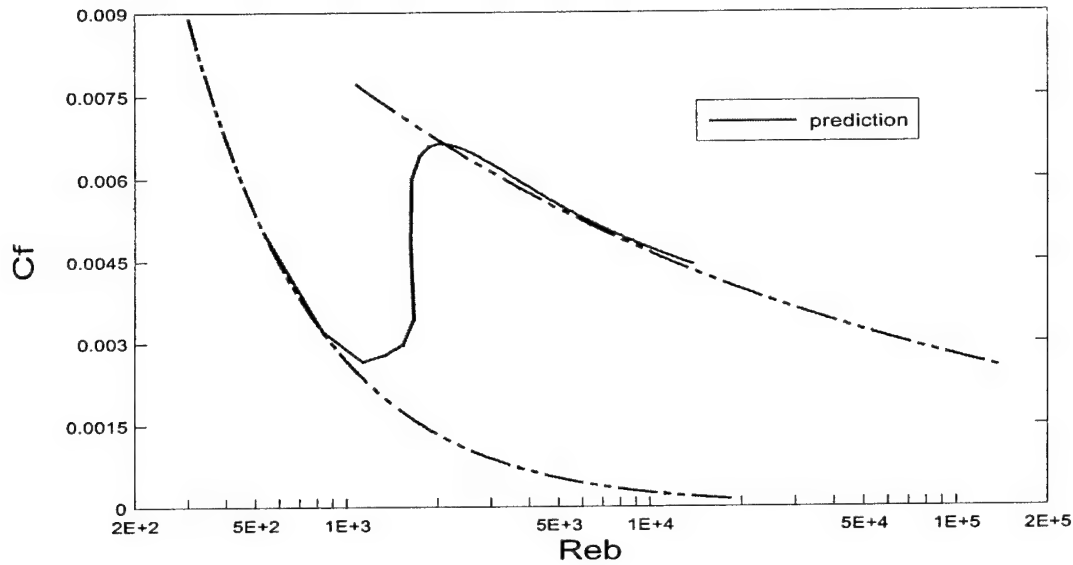


Figure 24. predictions of the skin friction in channel flow for various bulk Reynolds numbers. Dashed lines are fully laminar and fully turbulent correlations.

### 3.8 Conclusions

The ability of the turbulent potential model to predict transition in a wide variety of boundary layer flows has been demonstrated. This includes the ability to predict everything from natural transition (a first for RANS based models) to large free-stream turbulence intensities. The model is also demonstrated to be able to accurately calculate the transitional flat plate boundary layer under favorable and adverse pressure-gradients. The ability of this model to reflect the effect of noise on the natural transition is also shown by comparison with corresponding experimental data under different conditions. Finally, the relaminarization in turbulent channel flow is successfully captured using this model. The computation cost of the proposed method is comparable to the widely used two-equation models such as  $k/\epsilon$ . However, unlike  $k/\epsilon$ , the model does not assume equilibrium between the developing instability and/or turbulence fluctuations, and it is this non-equilibrium nature to which we attribute these successful predictions.

## 4. Large Eddy Simulation

This portion of the research demonstrates that the turbulent potential model can be used to model small scale turbulence in the context of a large eddy simulation. This is essentially using a RANS model to do LES. But in this context we must be very careful to delineate what is meant by a RANS model and LES because the formal definitions of these two modeling approaches makes them mutually exclusive. What we intend by the statement ‘RANS model in an LES context’ is the use of models which involve the solution of partial differential equations to obtain the unknowns necessary to close and solve the system. Standard LES subgrid scale models are algebraic in nature.

The use of RANS models in an LES context is not immediately intuitive from either the RANS or LES perspective. LES subgrid models have always had a focus on simplicity and low cost, and the solution of partial differential equations is rarely considered to be either. The construction of classic RANS models relies heavily on notions of turbulence universality and often turbulence equilibrium, both of which are harder to justify if we now restrict the model to represent only fluctuations below a subgrid threshold. Nevertheless, we intend in this section, to show the benefits of using just this counterintuitive approach. It

will be shown that some RANS models (such as the turbulent potential model) can be applied successfully well beyond their formal range of applicability and into the subgrid modeling regime.

The use of RANS models to perform large eddy simulation is not an entirely new idea. Deardorf (1973) used a Reynolds stress transport equation model in a LES of atmospheric turbulence. Soon after this, Schumann (1975) performed a large eddy simulation using a partial differential equation for the unresolved turbulent kinetic energy. More recently Glosal, Lund, & Moin (1995) have tested a one-equation LES model which also uses a kinetic energy evolution equation. They concluded that the model worked well, but that the additional cost incurred was not advantageous compared to traditional LES models. Fureby *et al.* (1997) have essentially reproduced Deardorf's earlier work using updated closure models, and have shown excellent results for isotropic decay and turbulent channel flow with only a 20% increase in computational cost over standard LES models. Speziale (1998) proposed a switch for the k/ε model that would allow it to smoothly transition into an LES subgrid scale model. Along similar lines, Spallart (2000) has demonstrated a switch for the Spallart-Allmaras (1992) model that allows it to smoothly transition from RANS to LES. The hybrid Spallart model is called detached eddy simulation (DES) because the switch is based on the distance to the wall, and therefore causes RANS type behavior near the wall and LES far away (for the detached eddies). A number of simulations based on both the Speziale and DES approaches have subsequently been performed (Peltier *et al.* 2000, Travin *et al.* 2000, Arunajatesan *et al.* 2000).

The fundamental difference between the proposed approach and the hybrid models of Speziale and Spallart is that the turbulent model does not require an explicit switch to do LES. This is actually a profound difference, but the importance of the distinction is very difficult to convey abstractly.

#### 4.1 Theoretical Approach

We start with the decomposition of the instantaneous velocity field  $V_i$ :

$$V_i = U_i(\lambda, t) + u_i \quad (4.1)$$

where  $U_i$  and  $u_i$  are the resolved and unresolved (modeled) velocities respectively. The resolved part  $U_i$  accounts for the flow motion of unsteady, energy containing scales and therefore is a function of wavenumber  $\lambda$  and time  $t$ . It also accounts for any steady, mean motion. The evolution equation for the resolved velocity field can be written as

$$\frac{\partial U_i}{\partial t} + U_j \frac{\partial U_i}{\partial x_j} + \frac{\partial \langle u_i u_j \rangle}{\partial x_j} = -\frac{\partial p_r}{\partial x_i} + \nu \frac{\partial^2 U_i}{\partial x_j \partial x_j} \quad (4.2)$$

where the angular bracket represents averaging over modeled scales. The resolved pressure  $p_r$  is defined by

$$-\frac{\partial p_r}{\partial x_i \partial x_i} = \frac{\partial U_i}{\partial x_j} \frac{\partial U_j}{\partial x_i} + \frac{\partial^2 \langle u_i u_i \rangle}{\partial x_j \partial x_j} \quad (4.3)$$

The primary variable to be numerically solved in this work is the stream function, so the pressure is only explicitly required at boundary cells. The sum of the last term on the r.h.s. of Equation (4.2) can be considered playing the same role as the convection term in the filtered momentum equation of a conventional LES method. Instead of using the filtering function to account for the contribution of the Reynolds stress tensor (Residual stress tensor) in the momentum equation, we stick to relating it to the turbulent potentials. So the equation (3.2) is rewritten as:

$$\frac{\partial U_i}{\partial t} + U_j \frac{\partial U_i}{\partial x_j} = -\frac{\partial p_r}{\partial x_i} + \nu \frac{\partial^2 U_i}{\partial x_j \partial x_j} - \varepsilon_{ijk} \frac{\partial \psi_k}{\partial x_j} - \frac{\partial \phi}{\partial x_i} \quad (4.4)$$

The flow motion above the grid scale should be resolved by the numerical solver, and evolve via equation (4.4), which can be closed by the TPM model solving for the small scale motions. The model equations can be found in the work of Zhang (2002) with a few modifications.

The transport equation for the resolved kinetic energy can be obtained by taking the dot product of (4.4) with the velocity vector.

$$\begin{aligned} \frac{\partial K_r}{\partial t} + U_j \frac{\partial K_r}{\partial x_j} = & -\frac{\partial}{\partial x_i} (U_i p_r) + \nu \frac{\partial}{\partial x_j} \left( U_i \frac{\partial U_i}{\partial x_j} \right) - \frac{\partial}{\partial x_i} (U_i \phi) \\ & - \nu \frac{\partial U_i}{\partial x_j} \frac{\partial U_i}{\partial x_j} - \varepsilon_{ijk} \frac{\partial \psi_k}{\partial x_j} U_i \end{aligned} \quad (4.5)$$

The evolution of the total resolved kinetic energy can be derived by the integrating equation (4.5) over the computational domain. Notice that the convection term on the l.h.s. and the first three terms on the r.h.s. just redistribute the kinetic energy inside the periodic domain. We end up with a compact form:

$$\frac{\partial}{\partial t} \left( \int K_r dv \right) = - \int \varepsilon_r dv - \int P_r dv \quad (4.6)$$

where the resolved dissipation term is  $\varepsilon_r = \nu \frac{\partial U_i}{\partial x_j} \frac{\partial U_i}{\partial x_j}$  and the resolved production term is

$P_r = \varepsilon_{ijk} \frac{\partial \psi_k}{\partial x_j} U_i$ . While this is called a production term because of its form, this term tends to reduce

the resolved kinetic energy (sending it to the unresolved kinetic energy). The evolution equation for the modeled kinetic energy was given by (4.5). The total modeled kinetic energy is governed by the following integral equation,

$$\frac{\partial}{\partial t} \left( \int K_m dv \right) = - \int \varepsilon_m dv + \int P_m dv \quad (4.7)$$

where the resolved production term is  $P_m = \omega_i \psi_i$  and  $\omega_i$  is a component of vorticity vector. Note that the production terms for the resolved and modeled energy equations are mathematically equivalent, though they were calculated in the CFD code in the different forms. This can be more easily seen from simple derivation,

$$\begin{aligned} \int P_r dv &= \int \varepsilon_{ijk} \frac{\partial \psi_k}{\partial x_j} U_i dv = \int \frac{\partial}{\partial x_j} (\varepsilon_{ijk} \psi_k U_i) dv - \int \varepsilon_{ijk} \frac{\partial U_i}{\partial x_j} \psi_k dv \\ &= \int \varepsilon_{kji} \frac{\partial U_i}{\partial x_j} \psi_k dv = \int \omega_k \psi_k dv \end{aligned} \quad (4.8)$$



## 4.2 Channel Flow

Shown below are various calculations using the turbulent potential model of turbulent channel flow at a shear velocity Reynolds number of 180. The channel flow is a very well understood flow, both in terms of LES models and DNS statistics of the flow. The low Reynolds number was chosen so that we could test the model right into the DNS limit. The domain is periodic in the streamwise and spanwise directions and only half the wall normal domain is simulated with a symmetry condition at the channel midplane. The result is therefore closer to an open channel flow simulation, but it is observed (Salvetti *et al.*, 1997) that this midplane boundary condition does not affect the wall boundary layer turbulent statistics.

Five cases were run with varying mesh resolutions in the spanwise and streamwise directions. The wall normal resolution of 60 points is required even for a pure RANS simulation of the channel if wall functions are not used, so the wall normal resolution was left unaltered. The simulations were initialized with random fluctuations and a uniform mean velocity in the streamwise direction. The simulation was then run until statistical steady state was achieved. A series of five simulations were run with all variables fixed except the spanwise and streamwise mesh resolution. Table 3.1, shows the resolutions for the various simulations and the resolution of the reference DNS simulation of Moser, Kim & Mansour (1999). The current simulations vary from DNS resolution to LES type resolutions to what should closely approximate RANS resolutions (where the near wall streaks can not possibly be resolved). Case 1 used an 80x60x80 Cartesian mesh. Each succeeding case doubles the streamwise and spanwise grid size so that Case 5 uses a 5x60x5 grid. Figure 25 shows the mean velocity profiles for all the simulations and the DNS results of Moser *et al.*

	Moser, Kim & Mansour	Case 1	Case 2	Case 3	Case 4	Case 5
$\Delta x^+$	17.7	18.0	36.0	72.0	144.0	288.0
$\Delta y_{\min}^+$	0.054	0.48	0.48	0.48	0.48	0.48
$\Delta z^+$	5.9	6.75	13.5	17.0	34.0	68.0
$\Delta x / h$	0.098	0.10	0.20	0.40	0.80	1.60
$(\Delta y / h)_{\max}$	0.024	0.014	0.014	0.014	0.014	0.014
$\Delta z / h$	0.033	0.037	0.075	0.15	0.30	0.60

Table 3.1: Mesh resolutions for calculations of channel flow using the turbulent potential model.

The important result demonstrated in figure 25 is that the turbulent potential model naturally adapts to any mesh resolution. The skin friction is within 3% of the DNS data for all cases. Case 1 is essentially DNS, the modeled turbulence quantities are all extremely small in this case. Case 2 is LES, the turbulent eddy viscosity is roughly the order of the laminar viscosity in this case. (Note that eddy viscosity is not used in the turbulent potential model but was calculated for these test cases as a simple way of evaluating the importance of the model on the resolved flow). Case 3 shows the most model overlap, the flow solution is still unsteady, but the flow is probably dominated by the model at this point. The eddy viscosity is up to ten times the laminar viscosity, and the resolved RMS levels are only a third of their DNS levels. Cases 4 and 5 are fully RANS simulations and display no unsteadiness or three-dimensionality at steady state.

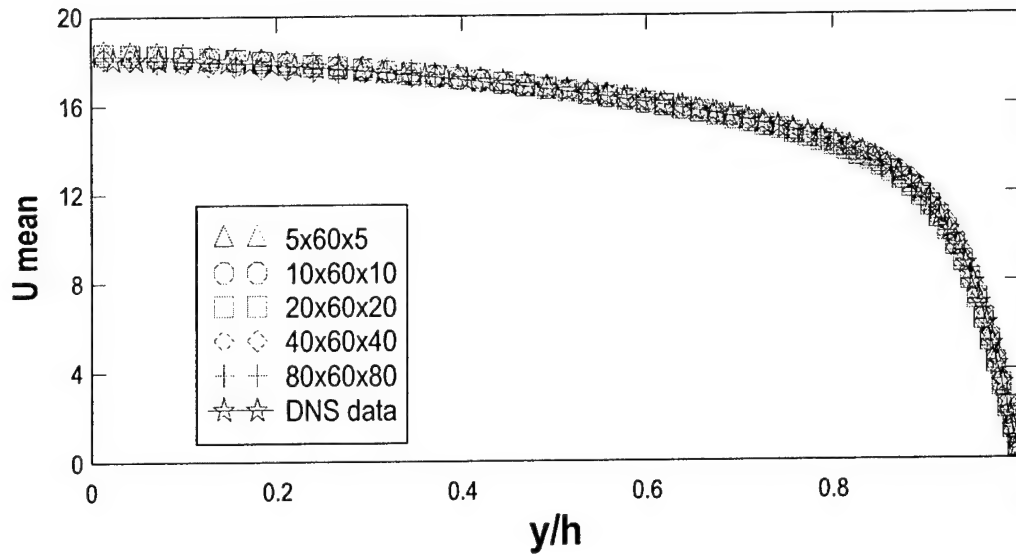


Figure 25. Calculations of mean velocity in a turbulent channel flow at  $Re_\tau = 180$  using the turbulent potential model. The mesh resolutions ranging from DNS to RANS, and are compared with the DNS data of Moser *et al.*

Note that hybrid models that are based on a switch (all existing ones) can not reproduce Figure 25. The explicit switch invariably alters the model in the coarse mesh limit resulting in mesh dependent results (see Nikitin *et al.* 2000). It is believed that the result presented above is closely tied to the non-equilibrium nature of the model. Tests of a low Reynolds number  $k/\epsilon$  model (not shown) indicated that  $k/\epsilon$  could not function in the LES and DNS regime unless the explicit Speziale damping switch was imposed. This switch invariably altered the coarse mesh solutions. It is hypothesized that Reynolds stress transport equations could reproduce Figure 25, but given the reduced cost and increased robustness of the turbulent potential model, the advantages of using a Reynolds stress transport model are limited.

A preliminary observation that was obtained from these simulations is that the transition from LES-like (large scale unsteadiness) to RANS-like (steady, one dimensional) solutions was relatively abrupt. This may be related to the low Reynolds number of the simulations, but Nikitin *et al.* report similar behavior with DES at much larger Reynolds numbers and suggests that the phenomena occurs when the mesh no longer can resolve the larger scale energy containing turbulent scales.

The turbulent potential model (like other hybrid approaches) solves the issue of how to perform LES near walls at high Reynolds numbers. Standard LES requires that turbulence producing structures be resolved. Near the wall the important structures are streaks which scale inversely with the Reynolds number. This means that standard LES of near wall turbulence which ought to be Reynolds number independent, is not. Significant efforts to generate wall functions, or discontinuous two layer models to avoid this Reynolds number dependence have lead to methods for the wall which display a great deal of complexity (Cabot & Moin 1999, Baggett 1997, Bagwell *et al.* 1993). LES models which have the ability to transition smoothly to a RANS limit (such as the proposed approach) can model near wall turbulence with only a possible logarithmic dependence on the Reynolds number.

Finally it should be noted that the fact that the proposed model can be applied in both the RANS and LES limits makes it extremely attractive to the end users of such models. The ability to use a whole range of modeling solutions within a single code and unified modeling framework greatly enhances the users ability to make the difficult choice between cost and accuracy that turbulence invariably imposes.

### 4.3 RANS Modeling of Isotropic Decaying Turbulence

All non-equilibrium models should work for isotropic turbulence before it is applied to other flows. A uniform  $64^3$  quadrilateral mesh is placed on a  $18\pi^3$  cubic domain. The domain is periodic in the streamwise, spanwise and lateral directions. We first tested the performance of the model in predicting the evolution of turbulence quantities during the decay. The initial condition is taken from a  $512^3$  simulation previously calculated by de Bruyn Kops (1998). This case is equivalent to the famous decay experiment of Comte-Bellot and Corrsin (1971). The flow has an initial turbulent kinetic energy of  $753 \text{ (cm}^2/\text{s}^2)$  and the initial dissipation rate of the value  $4487 \text{ (cm}^2/\text{s}^3)$ . This initial condition matches the laboratory kinetic energy at  $x/M = 42$  where  $M$  is the grid space in the experiment.

The model was tested under the condition that the resolved velocity is negligible. This is a full RANS simulation, with no perceptible resolved flow, even though the mesh is  $64^3$ . The prediction of present model was shown in Figure 26 and it is consistent with the DNS data of de Bruyn Kops.

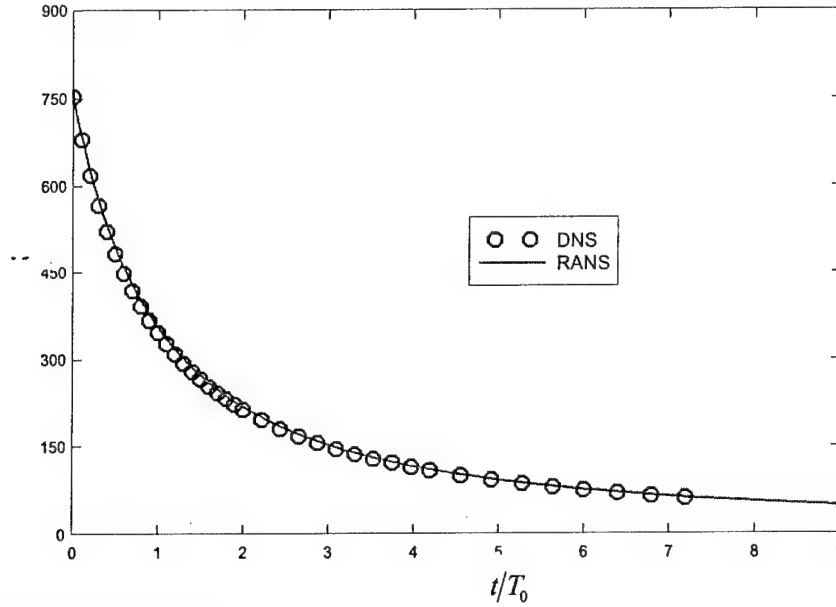


Figure 26. RANS simulation

### 4.4 LES of Isotropic decaying turbulence

This simulation took a  $64^3$  truncation of the  $512^3$  velocity field computed by de Bruyn Kops (1998) as the initial condition for the resolved flow field. This velocity field was generated in a series of process so that the initial energy spectrum matches the experiment and the large-scale structures are properly developed. The contour plot of the initial resolved velocity component is shown in Figure 27.

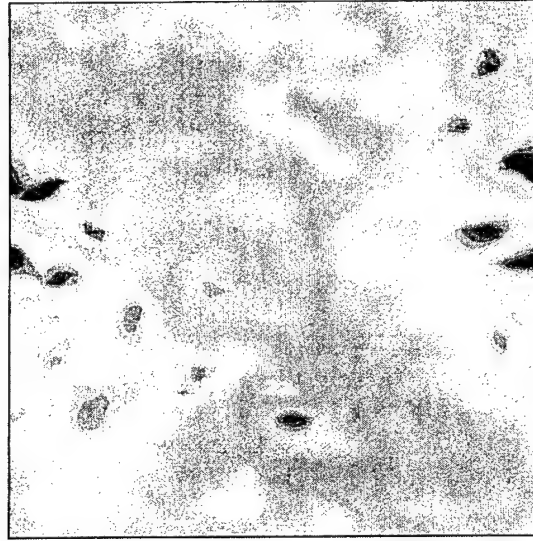


Figure 27. Velocity contour of initial isotropic turbulence

It can be calculated that the initial values for the resolved kinetic energy and initial resolved dissipation are  $552 \text{ (cm}^2/\text{s}^2 \text{)}$  and  $395 \text{ (cm}^2/\text{s}^3 \text{)}$  respectively. To match the total initial kinetic energy and initial dissipation rate of the experiment, the initial values of the modeled turbulence quantities are taken to be  $201 \text{ (cm}^2/\text{s}^2 \text{)}$  for the kinetic energy and  $4192 \text{ (cm}^2/\text{s}^3 \text{)}$  for the dissipation rate. The decay of the resolved, modeled and total kinetic energies are plot in Figure 28 together with the result from de Bruyn Kops (1998) for comparison. The variation of time scale  $k/\varepsilon$  is plotted in Figure 29. For all cases, the time variable was non-dimensionalized with respect to the initial eddy turnover time  $T_0 = K_0 / \varepsilon_0$ .

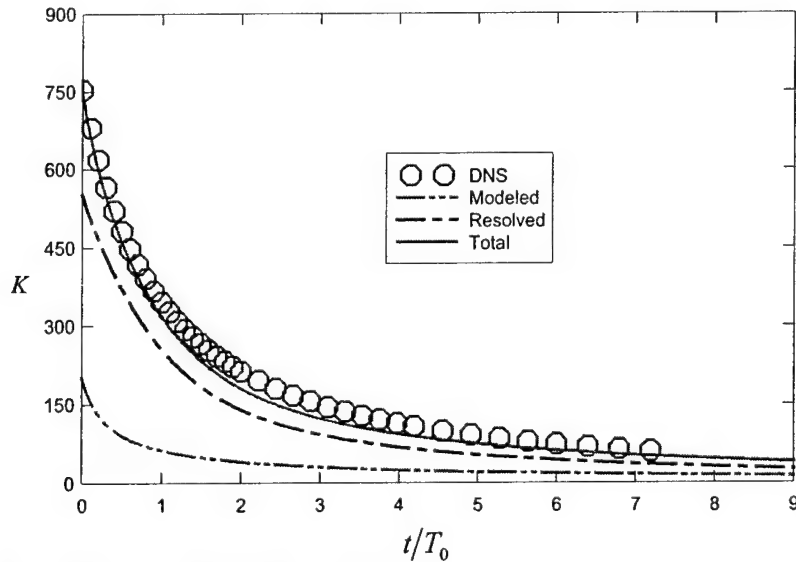


Figure 28. Comparison of the kinetic energy decaying

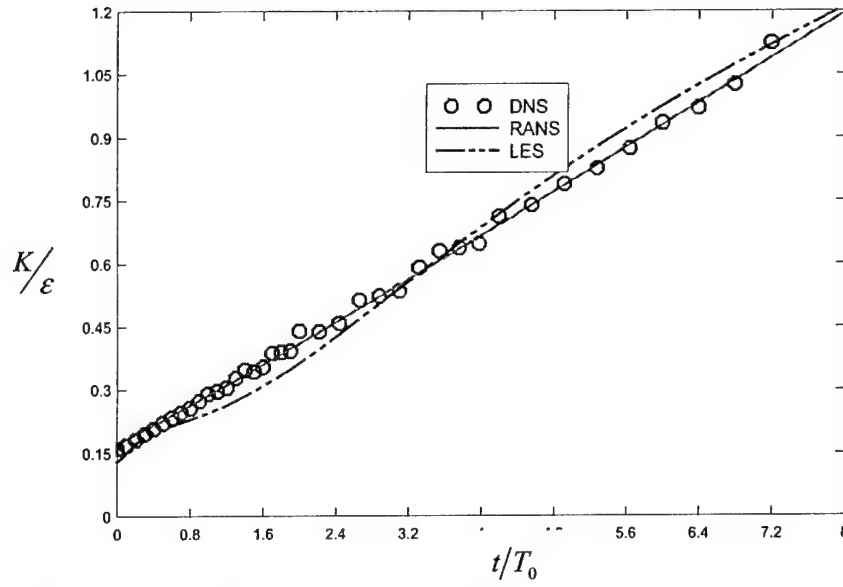


Figure 29 Comparison of the evolution of time scale

The decay of the total kinetic energy agrees well with the DNS data in the early and end stages of the simulation. The reason for the discrepancy in the middle range is under investigation. It was found that the decay rate of the resolved scales is affected significantly by the way it communicates with the modeled scales in the actual CFD code. So hopefully improvement in the numerical scheme for the resolved flow field will produce a more reasonable solution.

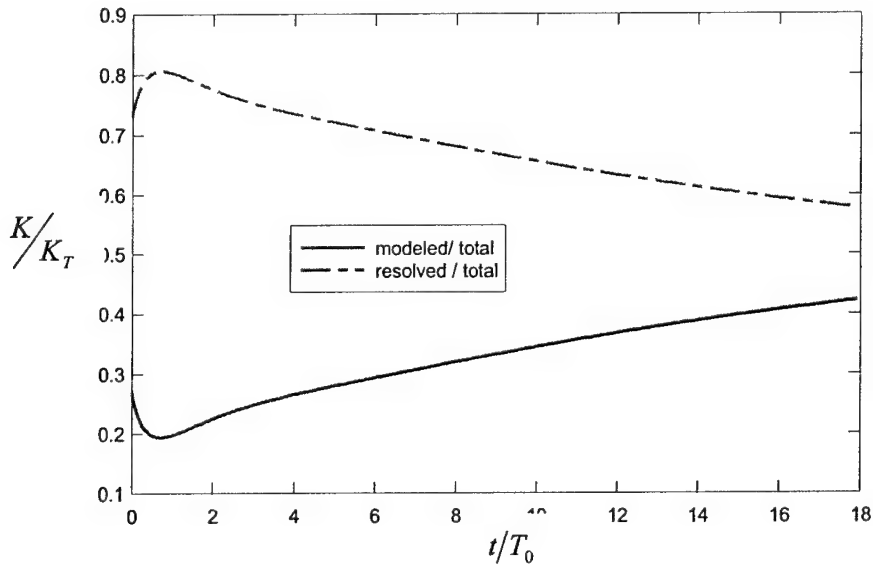


Figure 30. The fracture of kinetic energies

Figure 29 should be linear. The results of DNS and the RANS model are indeed linear. The LES simulation is not linear and is the focus of the investigation. Figure 30 is the ratios of modeled and resolved kinetic energies to the total kinetic energy. It can be observed that the ratio of the modeled portion is increasing

rapidly. This implies that the modeled scales might be excessively energetic. The similar trend was reported by Girimaji (2002) and considered unphysical.

Figure 31 and Figure 32 show the evolution of production and dissipations respectively. The resolved and modeled production terms match each other exactly as expected. The magnitude of the modeled dissipation is much bigger than its resolved counterpart but the latter wins quickly over the later stage. The resolved dissipation also starts to decrease in magnitude soon after that.

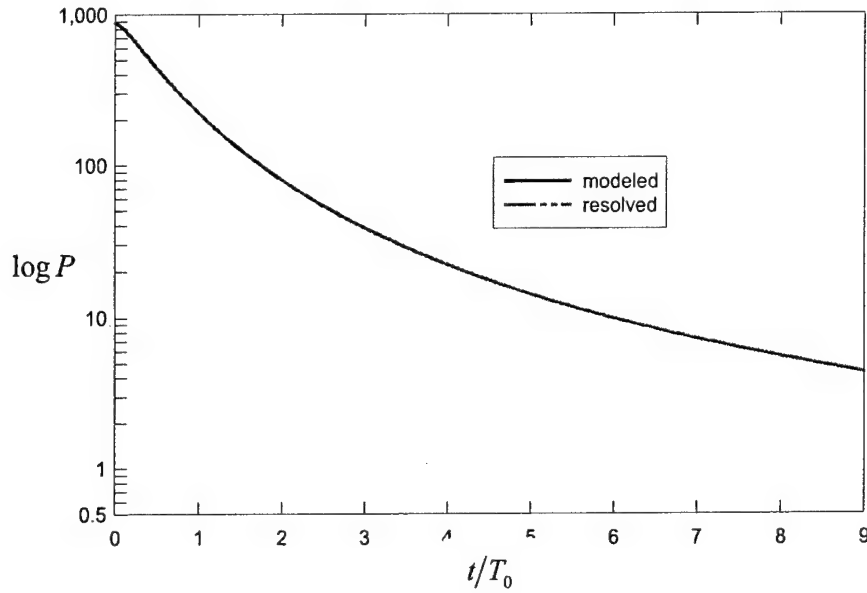


Figure 31 Evolution of Productions

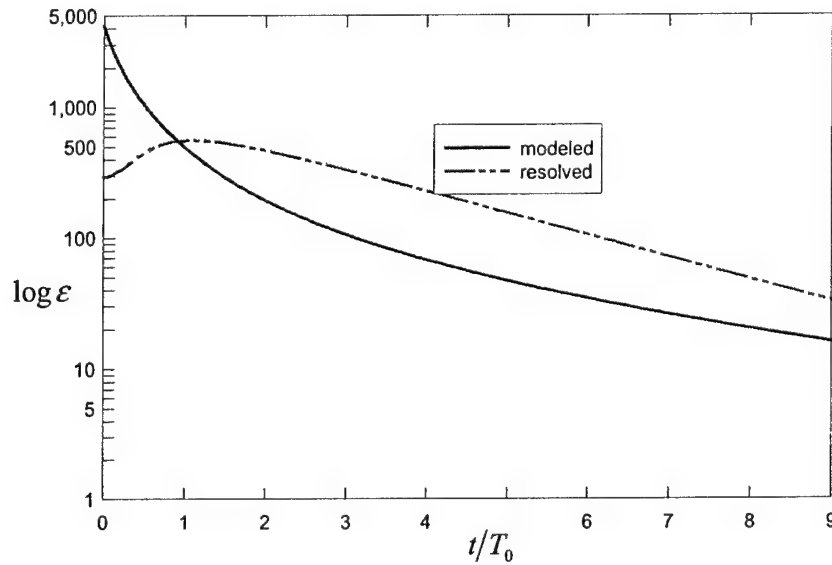


Figure 32 Evolution of Dissipation

The derivatives of resolved and modeled kinetic energies are plotted in Figure 33 with the evolution of  $-\int \varepsilon_r dv - \int P_r dv$  and  $-\int \varepsilon_m dv + \int P_m dv$  (the r.h.s of equation 4.6 and 4.7 respectively). From this picture, it can be seen that the conservation of energy was correctly captured by the numerical computation. It is not clear whether the resolved dissipation was calculated accurately enough.

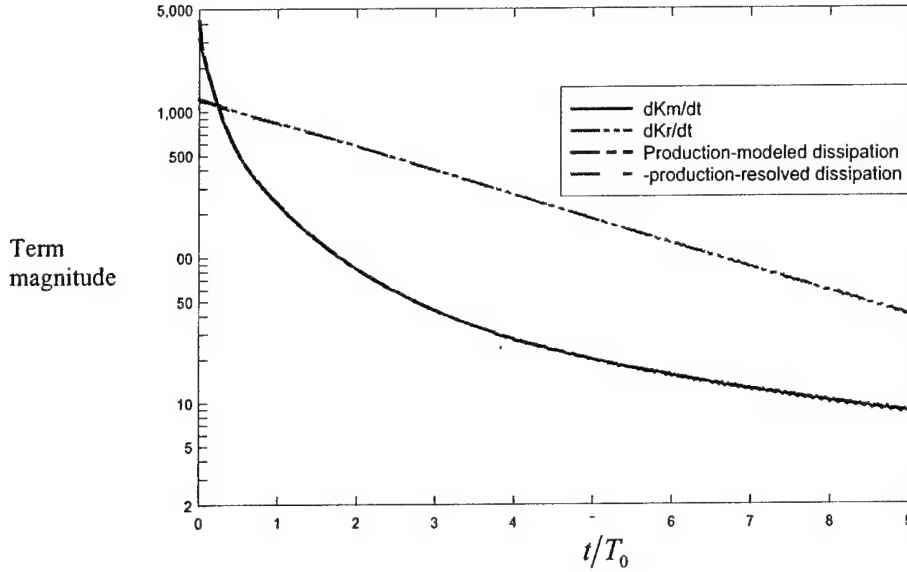


Figure 33. Conservation of energy equation terms

## 4.5 Conclusion

The simulation results have shown that the turbulence potential model, when implemented as a pure RANS model, is able to produce predictions in accordance with DNS for the isotropic decaying turbulence. When the model is used as a LES model, the results are fairly close to the DNS data, but could use further improvement.

The modeled scales tend to be over energetic in the late stage. The reason is under investigation. A control parameter relating to the proportion of the modeled kinetic energy is considered to be used to yield the desired solution

An important issue in LES is the correct transfer of kinetic energy between the resolved and modeled (residual) flow field. Globally, energy is transferred from the large scales to the small scales. Nevertheless, the production in the modeled scales can be negative locally and backscatter transfer can happen. The modeled initial kinetic energy will be set a large value while the resolved part is initially small. We will expect the resolved energy can be fed by the decaying modeled part and rise up to a certain value.

## 5. Conclusion

This three year project to evaluate the turbulent potential model's ability to predict rotation, turbulent transition, and sub-grid scale turbulence has been very successful. The correct mathematical framework for implementing rotation was determined, a wide variety of boundary layer transition cases were predicted, and the possibility of using the model for LES was explored. In summary, it has not only been demonstrated that the turbulent potential model is competitive with existing RANS models, it has been shown that the model can be applied to situations usually considered to be outside the realm of RANS models.

## Appendix

### A1.0 Frame invariant quantities and frame consistent equations

*Frame consistency* in the context of turbulence modeling can be defined as the property of the model to yield the same solution regardless of the non-inertial frame from which it is being computed. *Frame invariant* quantities are quantities which do not change from one non-inertial frame to another. It can be said that frame consistency is defined in the context of equations, while frame invariance is defined in the context of quantities like tensor fields and vector fields.

We consider a reference frame (\*) which is in a state of arbitrary time dependent rotation with respect to a fixed inertial frame and with the same origin. The position of a point with respect to the rotating and fixed frames are given by  $\mathbf{x}^*$  and  $\mathbf{x}$  respectively. Now

$$\mathbf{x}_k^* \mathbf{e}_k^* = \mathbf{x}_m \mathbf{e}_m \quad (0.1)$$

where  $\mathbf{e}_m$  and  $\mathbf{e}_k^*$  are the unit vectors representing the axes of the fixed and the moving reference frame respectively. The relationship between  $\mathbf{e}_m$  and  $\mathbf{e}_k^*$  can be given by

$$\mathbf{e}_k^* = T_{km} \mathbf{e}_m \quad (0.1)$$

where  $\mathbf{T}$  is a time dependent orthogonal (or unitary) transformation matrix describing the rotation. Thus, from (0.1) and **Error! Reference source not found.** we can say that

$$\mathbf{x}^* = \mathbf{T} \mathbf{x} \quad (0.2)$$

If we differentiate this with respect to time then we get

$$\dot{\mathbf{x}}^* = \mathbf{T} \dot{\mathbf{x}} + \dot{\mathbf{T}} \mathbf{x} \quad (0.3)$$

Taking an average we get

$$\bar{\dot{\mathbf{x}}}^* = \mathbf{T} \bar{\dot{\mathbf{x}}} + \dot{\mathbf{T}} \mathbf{x} \quad (0.4)$$

Subtracting (0.4) from (0.3), and then invoking (0.1), we get

$$\mathbf{u}^* = \mathbf{T} \mathbf{u} \quad (0.5)$$

which is the definition of a frame invariant vector. From (0.3) and (0.4) we can see that the total and mean velocity fields are *not* frame invariant. It may be easier to understand the meaning of frame invariance if we

take  $\mathbf{T} = \mathbf{I}$ , the identity matrix, at a certain instance of time. In that case,  $\dot{\mathbf{x}}^* = \dot{\mathbf{x}} + \dot{\mathbf{T}} \mathbf{x}$  and  $\mathbf{u}^* = \mathbf{u}$ . Which means that the fluctuating velocity is the same when it is seen from two frames overlapped on each other, but the velocity transformation is dependent on the frame rotation rate. Thus, to get the components of a frame invariant vector in a different frame, we simply project the vector onto axes of the different frame. However a vector which is not frame invariant changes from one frame to another. The Reynolds stress



tensor can be shown to be frame invariant (Speziale (1970)), though the criterion for frame invariance changes since it is a second order tensor:

$$\mathbf{R}^* = \mathbf{T} \mathbf{R} \mathbf{T}^T \quad (0.6)$$

The Reynolds stress tensor transport equation has the material derivative of the Reynolds stress on the left hand side of the equation. The material derivative of the Reynolds stress is not a frame invariant quantity. We can show this through the following steps, which are written in Cartesian tensor notation. From (0.2)

$$x_i^* = T_{ik} x_k \quad (0.7)$$

Multiplying both sides by  $T_{im}$  we get

$$T_{im} x_i^* = T_{im} T_{ik} x_k \quad (0.8)$$

Now since  $\mathbf{T}$  is an orthogonal matrix, therefore  $T_{im} T_{ik} = \delta_{mk}$ , and hence

$$x_m = T_{im} x_i^* \quad (0.9)$$

Therefore we finally have the relation

$$\frac{\partial x_m}{\partial x_i^*} = T_{im} \quad (0.10)$$

and the chain rule

$$\frac{\partial}{\partial x_k^*} = T_{kl} \frac{\partial}{\partial x_l} \quad (0.11)$$

Similarly, for the time derivative we can invoke (0.9) and the fact that  $t^* = t$  and get

$$\begin{aligned} \frac{\partial}{\partial t^*} &= \frac{\partial t}{\partial t^*} \frac{\partial}{\partial t} + \frac{\partial x_k}{\partial t^*} \frac{\partial}{\partial x_k} \\ &= \frac{\partial}{\partial t} + \frac{\partial T_{mk} x_m^*}{\partial t^*} \frac{\partial}{\partial x_k} \\ &= \frac{\partial}{\partial t} + \dot{T}_{mk} x_m^* \frac{\partial}{\partial x_k} \end{aligned} \quad (0.12)$$

Now, we find out the transformation for the material derivative operator

$$\frac{\partial}{\partial t^*} + \bar{v}_k^* \frac{\partial}{\partial x_k^*} = \frac{\partial}{\partial t} + \dot{T}_{ml} x_m^* \frac{\partial}{\partial x_l} + T_{kl} v_k^* \frac{\partial}{\partial x_l} \quad (0.13)$$

Using (0.13) and (0.4)

$$\frac{\partial}{\partial t^*} + \bar{v}_k \frac{\partial}{\partial x_k} = \frac{\partial}{\partial t} + \bar{v}_k \frac{\partial}{\partial x_k} \quad (0.14)$$

It can be immediately seen that a material derivative operated on a scalar quantity will be frame invariant. Now we operate it on the Reynolds stress tensor. Using (0.14) and (0.6) we can get

$$\begin{aligned} \frac{\partial R_{ij}^*}{\partial t^*} + \bar{v}_k \frac{\partial R_{ij}^*}{\partial x_k} &= \frac{\partial T_{im} R_{mn} T_{jn}}{\partial t} + T_{im} T_{jn} \bar{v}_k \frac{\partial R_{mn}}{\partial x_k} \\ &= \{ \dot{T}_{im} T_{jn} + T_{im} \dot{T}_{jn} \} R_{mn} + T_{im} T_{jn} \dot{R}_{mn} + T_{im} T_{jn} \bar{v}_k \frac{\partial R_{mn}}{\partial x_k} \end{aligned} \quad (0.15)$$

Clearly, the material derivative is not frame invariant when it is operated on a second order tensor.

Oldroyd (1950) proposed a derivative in order to get a time rate of change of a tensor with respect to a coordinate system getting convected and distorted along with the deforming fluid. This gives a derivative which is frame invariant. The Oldroyd derivative of the Reynolds stress tensor is given by

$$\frac{\delta R_{ij}}{\delta t} = \frac{\partial R_{ij}}{\partial t} + \bar{v}_k \frac{\partial R_{ij}}{\partial x_k} - R_{ik} \frac{\partial \bar{v}_j}{\partial x_k} - R_{jk} \frac{\partial \bar{v}_i}{\partial x_k} \quad (0.16)$$

It can be noted that the third and the fourth terms are new when compared to the material derivative. Using steps similar to those used from (0.7) to (0.15), we can verify (Appendix A) that

$$\frac{\delta R_{ij}^*}{\delta t^*} = T_{im} T_{jn} \frac{\delta R_{mn}}{\delta t} \quad (0.17)$$

where  $\frac{\delta}{\delta t}$  is being used to denote the Oldroyd derivative. A very important point to be noted is that the operation of an Oldroyd derivative on a tensor gives a frame invariant quantity only if the tensor itself is frame invariant. Similar definition holds for the Oldroyd derivative of a vector.

### A1.1 Some frame invariant velocity-field dependent quantities

The following velocity-field dependent tensors are frame invariant (Fredrickson (1964)). These are the strain and the intrinsic vorticity. The strain tensor  $S$  is defined as

$$S_{mn} = \frac{1}{2} (\bar{v}_{m,n} + \bar{v}_{n,m}) \quad (0.18)$$

While the intrinsic vorticity tensor  $\hat{W}$  is defined as

$$\hat{W}_{mn} = W_{mn} + e_{nmk} \Omega_k \quad (0.19)$$

Here

$$W_{mn} = \frac{1}{2}(\bar{v}_{m,n} - \bar{v}_{n,m}) \quad (0.20)$$

is the conventional vorticity tensor.

### A1.2 Frame consistent equations for Reynolds stresses and turbulent potentials

If we use an Oldroyd derivative on the left hand side of the exact RST equation, then we get

$$R_{ij,t} + \bar{v}_k R_{ij,k} + P_{ij} = 2\hat{P}_{ij} + \pi_{ij} - \varepsilon_{ij} + C_{ijk,k} + \nu R_{ij,kk} \quad (0.21)$$

Here we have a new production term, which includes the Coriolis term

$$\begin{aligned} \hat{P}_{ij} &= -R_{ik} \bar{v}_{j,k} - R_{jk} \bar{v}_{i,k} - e_{jmk} R_{ik} \Omega_m - e_{imk} R_{jk} \Omega_m \\ &= -R_{ik} (\hat{W}_{jk} + S_{jk}) - R_{jk} (\hat{W}_{ik} + S_{ik}) \end{aligned} \quad (0.22)$$

The new production term is a frame invariant quantity because it involves the intrinsic vorticity tensor and strain tensor. On the contrary  $P_{ij}$  is not a frame invariant quantity. As shown by Speziale (1979), the Reynolds stress, pressure strain, dissipation, turbulent diffusion and viscous diffusion can also be found to be frame invariant quantities.

Thus the left hand side of (0.21) is frame invariant because it is equal to the Oldroyd derivative while all the terms on the right hand side of (0.21) are frame invariant, from the discussion in the previous paragraph. There are two things to be inferred from this. Firstly, the exact RST equation is frame consistent. Secondly, any Reynolds stress transport model will be material frame consistent if an Oldroyd derivative is used on the left hand side, and frame invariant terms are used on the right. Now we go on to try and find out a similar criterion for the transport equations of the turbulent potentials to be frame consistent.

We first assume the turbulent potentials to be frame invariant quantities. Then we check whether this assumption gives equations which have the correct form. If that is true, then turbulence potentials are frame invariant quantities.

The assumption that turbulent potentials are frame invariant means that

$$\begin{aligned} \phi^* &= \phi \\ \psi_i^* &= T_{ik} \psi_k \end{aligned} \quad (0.23)$$

and

$$\frac{\partial^2 \phi^*}{\partial x_k^* \partial x_k^*} = \frac{\partial}{\partial x_m^*} \left\{ \frac{\partial R_{mn}^*}{\partial x_n^*} \right\} \quad (0.24)$$

$$\frac{\partial^2 \psi_i^*}{\partial x_k^* \partial x_k^*} = -\varepsilon_{iqm}^* \frac{\partial}{\partial x_q^*} \left\{ \frac{\partial R_{mn}^*}{\partial x_n^*} \right\} \quad (0.25)$$

If the chain rules (0.9) to (0.11) along with (0.6) and (0.23) are inserted in (0.24) and (0.25), then we get back equations which have exactly the same form as (0.24) and (0.25), but with quantities which are in the original untransformed frame of reference.

Since the turbulent potentials are frame invariant, therefore the Oldroyd derivative of the turbulence potentials will be a frame invariant quantity. Thus a reliable way to construct a frame consistent model using turbulence potentials is to use the Oldroyd derivative on the left hand side of the equation (transport terms), and ensure that all the terms on the right hand side (model terms) are frame invariant. The equation for the turbulence potentials now take the form

$$\frac{\partial \phi}{\partial t} + \bar{v} \cdot \nabla \phi = 2\hat{P}_\phi + \pi_\phi + \nabla \cdot \mathbf{C}_\phi - \epsilon_\phi + \nu \nabla^2 \phi \quad (0.26)$$

$$\frac{\partial \Psi}{\partial t} + \bar{v} \cdot \nabla \Psi - \Psi \cdot \nabla \bar{v} = 2\hat{P}_\Psi + \pi_\Psi + \nabla \cdot \mathbf{C}_\Psi - \epsilon_\Psi + \nu \nabla^2 \Psi \quad (0.27)$$

Here the main symbols on the right hand side in (0.26) and (0.27) have the same meaning as the symbols in (0.21), i.e.  $P$  denotes frame invariant production,  $\pi$  denotes pressure strain,  $C$  denotes turbulent diffusion, and  $\epsilon$  denotes the dissipation. The equation for  $\phi$  is a scalar equation, while the equation for  $\Psi$  is a vector equation. The Oldroyd derivative for  $\phi$  is the familiar material derivative, while that for  $\Psi$  is equal to material derivative in 2D flows and for flows which are inhomogeneous in only one direction.

A small point is to be noted when the Oldroyd derivative of  $R_{12}$  and  $\psi_3$  is compared. The Oldroyd derivative of  $R_{12}$  is

$$\frac{\delta R_{12}}{\delta t} = \frac{\partial R_{12}}{\partial t} + \bar{v}_2 \frac{\partial R_{12}}{\partial x_2} - R_{22} \frac{\partial \bar{v}_1}{\partial x_2} \quad (0.28)$$

While the Oldroyd derivative of  $\Psi_3$  is

$$\frac{\delta \Psi_3}{\delta t} = \frac{\partial \Psi_3}{\partial t} + \bar{v}_2 \frac{\partial \Psi_3}{\partial x_2} \quad (0.29)$$

The equations for  $\Psi_3$  and  $R_{12}$  should be the same because the quantities are equal to each other in flows with only one inhomogeneous direction. Therefore, the third term in the  $R_{12}$  equation must appear on the right hand side of (0.27). The only way that can be true is if that term can be written as a frame invariant vector. This is done by writing  $R_{22} \bar{v}_{1,2}$  as  $2\phi S_{12}$ . For a flow with only one direction of inhomogeneity we replace this term by the vector  $-\phi s$ , where  $s$  is a frame invariant term to be defined shortly. In this way we can ensure identical frame consistent equations for  $R_{12}$  and  $\Psi_3$  in flows with one direction of inhomogeneity, where they are equal to each other.

## References

- B. J. Abu-Ghannam & R. Shaw, "Natural Transition of Boundary Layers---The Effects of Turbulence, Pressure Gradient, and Flow History", *Journal of Mechanical Engineering Science*, **22** (5), pp. 213-228, 1980
- S. Are, X. Zhang & J. B. Perot, "Accuracy and Conservation properties of a three dimensional unstructured staggered mesh scheme for fluid dynamics", *International Journal of Rotating Machinery*, Accepted September 2001
- Bardina, J., Ferziger, J.H., & Reynolds, W.C. (1983). Improved turbulence models based on large eddy simulation of homogenous, incompressible turbulent flows. Stanford University Tech. Rep., TF-19.
- Bertoglio, J.P. (1982). Homogenous turbulent field within a rotating frame. *AIAA J.* **20**, 1175.
- Campbell, S., Dasey, T., Freehart, R., Heinrichs, R., Matthews, M., & Perras, G.H. (1996). Wake Vortex field measurement program at Memphis, AIAA Paper 96-0399.
- Chasnov, J.R. (1997). Decaying turbulence in two and three dimensions. In C. Liu & Z. Liu (ed.), *Advances in DNS/LES*. Ohio: Greyden Press.
- A. J. Chorin, "Numerical solution of the Navier-Stokes equations", *Math. Comput.*, **22**, 745, 1968.
- G. Comte-Bellot & S. Corrsin, "Simple Eulerian Time Correlation of Full and Narrow-band Velocity Signals in Grid-generated, 'Isotropic' Turbulence", *J. Fluid Mech.* **48**, pp. 273-?, 1971
- J. Coupland, ERCOFTAC Special Interest Group on Laminar to Turbulent Transition & Retransition T3A & T3B Test cases, 1990
- J. Coupland, ERCOFTAC Special Interest Group on Laminar to Turbulent Transition & Retransition T3C Test cases, 1990.
- Crow, S. (1968). Viscoelastic properties of fine-grained turbulence. *J. Fluid Mech.*, **33**, 1-20.
- Daly, B.J., & Harlow, F.H. (1970). Transport equations in turbulence. *Phys. Fluids*, **13**, 2634-2649.
- R. B. Dean, "Reynolds Number Dependence of Skin Friction and Other Bulk Flow Variables in Two-Dimensional Rectangular Duct Flow", *J. Fluids Eng.* **100** (6), pp. 215-223, 1978
- S. M. de Bruyn Kops & J. J. Riley, "Direct Numerical Simulation of Laboratory Experiments in Isotropic Turbulence", *Phys. Fluids*, **10** (9), pp. 2125-2127, 1998.
- S. Dhawan & R. Narasimha, "Some Properties of Boundary-layer Flow during the Transition from Laminar to Turbulent Motion", *J. Fluid Mech.* **3**, pp. 418-436, 1958
- J. K. Dukowicz & A. S. Dvinsky, "Approximation factorization as a high order splitting for the implicit incompressible flow equations", *J. Comput. Phys.*, **102**, 336-347 1992.
- H. W. Emmons, "The Laminar-Turbulent Transition in a Boundary Layer: Part I", *J. Aeronaut. Sci.*, vol. **18**, pp. 490-498.
- Fredrickson A.G. (1964). Principles and applications of rheology. New Jersey: Prentice Hall, Inc.
- Gatski, T.B., & Speziale, C.G. (1993). On explicit algebraic stress models for complex turbulent flows. *J. Fluid Mech.*, **254**, 59-78.

- V. Girault & P. Raviart, *Finite Element Approximation of the Navier-Stokes Equations*, Springer-Verlag, Berlin, 1986.
- S. S. Girimanji, "Unsteady RANS Method for Turbulence: Fundamentals and Model Development", Paper submitted to *J. Fluid Mech.*, 2002
- Govindaraju, S.P., & Saffman, P.G. (1971) Flow in a turbulent trailing vortex. *Physics of Fluids*, 14, (10), 2074-2080
- P. M. Gresho & S. T. Chan, "On the theory of semi-implicit projection methods for viscous incompressible flow and its implementation via a finite element method that also introduces a nearly consistent mass matrix, part 2: Implementation", *Int. J. Numer. Methods Fluids*, 11, pp. 621-659, 1990.
- C. A. Hall, J. C. Cavendish & W. H. Frey, "The dual variable method for solving fluid flow difference equations on Delaunay Triangulations", *Computers & Fluids*, 20 (2), pp. 145, 1991.
- Hallback, M. (1993). Development of Reynolds stress closures of homogenous turbulence through physical and numerical experiments. Doctoral thesis, Department of Mechanics, Royal Institute of Technology, Stockholm.
- F. H. Harlow & J. E. Welch, "Numerical calculations of time dependent viscous incompressible flow of fluid with a free surface", *Phys. Fluids*, 8 (12), pp. 2182-2189, 1965.
- J. M. Hyman & M. Shashkov, "The orthogonal decomposition theorems for mimetic finite difference methods", *SIAM J. on Num. Anal.*, 36 (3), pp. 788-818, 1999.
- Imao, S., & Itoh, M. (1996). Turbulent characteristics of the flow in an axially rotating pipe. *Int. J. Heat and Fluid Flow*, 17, 44-451.
- R. G. Jacobs & P. A. Durbin, "Simulations of Bypass Transition", *J. Fluid Mech.* 428, pp. 185-212, 2001
- L. Keffe, P. Moin & J. Kim, "The Dimension of Attractors Underlying Periodic Turbulent Poiseuille Flow", *J. Fluid Mech.* 242, pp. 1-29, 1992
- Jones, W.P., & Launder, B.E. (1972). The prediction of laminarization with a two-equation model of turbulence. *Int. J. Heat Mass Transfer*, 15, 301-314.
- Kristoffersen, R., & Andersson, H.I. (1993). Direct simulations of low-Reynolds-number turbulent flow in a rotating channel. *J. Fluid Mech.*, 256, 163-197.
- Launder, B.E., Reece, G.J., & Rodi, W. (1975). Progress in the development of a Reynolds stress turbulence closure. *J. Fluid Mech.*, 68, 537-566.
- B. E. Launder & B. I. Sharma, "Application of the Energy Dissipation Model of Turbulence to the Calculation of Flow Near a Spinning Disc", *Lett. Heat Mass Transfer*, 1, pp. 131-138, 1974.
- Lezius, D.K., & Johnston, J.P. (1976). Roll-cell instabilities in rotating laminar and turbulent channel flows. *J. Fluid Mech.*, 77, 153-175.
- D. K. Lilly, "On the computational stability of numerical solutions of time-dependent non-linear geophysical fluid dynamics problems", *Mon. Weather Rev.*, 93, pp. 11-26 1965.
- Lumley, J.L. (1978). Computational modeling of turbulent flows. *Adv. Appl. Mech.*, 18, 123-176.

- Matsumoto, A., Nagano, Y. & Tsuji, T. (1991). Direct numerical simulation of homogeneous turbulent shear flow. 5th Symposium on Computational Fluid Dynamics, Tokyo, 361-364
- Naot, D., Shavit, A. & Wolfshtien, M. (1970). Interactions between components of the turbulent velocity correlation tensor due to pressure fluctuations. *Israel J. Technol.*, 8, 259-269.
- Oberlack, M., Cabot, W. & Rogers, M.M. (1998). Group Analysis, DNS and modeling of a turbulent channel flow with streamwise rotation. Center for turbulence Research Proceedings of the Summer Program 1998.
- Oldroyd, J.G. (1950). On the formulation of rheological equations of state. *Proc. Roy Soc.*, A200, 523.
- S. Orszag, "Accurate solution of the Orr-Sommerfeld stability equation", *J. Fluid Mech.* **50**, pp. 689-703, 1971
- J. B. Perot, "An analysis of the fractional step method", *J. Comput. Phys.*, **108**, 51-58 1993.
- J. B. Perot, "Turbulence modeling using body force potentials", *Phys. Fluids*, **11** (9), pp. 2645-2656, 1999.
- J. B. Perot, "Conservation properties of unstructured staggered mesh schemes", *J. Comput. Phys.*, **159**, pp. 58-89 2000.
- J. B. Perot & J. Taupier, "Modeling Three-Dimensional Boundary Layers Using the Turbulent Potential Model", *AIAA 2000-0914*, Reno, Nevada, Jan, 2000
- J. B. Perot & H. Wang, "Modeling Separation and Reattachment Using the Turbulent Potential Model", *Proceedings of the 4<sup>th</sup> International Conference on Turbulence Modeling and Measurements*, Corsica, France, May, 1999
- Perot, J.B., & Moin, P. (1996). A new approach to turbulence modeling. Center for turbulence research Proceedings of the summer Program 1996.
- Perot, J.B. (1999). Turbulence modeling using body force potentials. *Physics of Fluids*, **11** (9), 2645-2656.
- Perot, J.B., & Moin, P. (1992). A near-wall model for the dissipation tensor, *Proceedings of the 11<sup>th</sup> Australasian Fluid Mechanics Conference*, University of Tasmania, Hobart., 471-474.
- Pope, S.B. (2000). *Turbulent Flows*, Cambridge University Press
- Rotta, J. (1951). Statistische Theorie nichthomogener Turbulenz I, *Z. für Physik*, **129**, 547-572.
- J. Rotta, "Statistische Theories nichthomogener Turbulenz I", *Z. Phys.* **129**, pp547-?, 1951
- W. C. Reynolds and S. C. Kassinos, "One-point modeling of rapidly deformed homogeneous turbulence", *Proceedings of the Royal Society of London A*, **451**, *Osborne Reynolds Centenary Volume*, pp. 87-104, 1995
- A. M. Savill, "A synthesis of T3 Test Case Predictions", *Numerical simulation of unsteady flows and transition to turbulence*, Pironneau, Rodi, Ryming, Savill, Truong, eds. Cambridge Press, 1990.
- A. M. Savill, Chapter 6, *Turbulence and Transition Modelling*, Hallback, Henningson, Johansson & Alfredsson, eds. Kluwer Academic Publishers, 1996
- G. B. Schubauer & P. S. Klebanoff, "Contribution to the mechanism of boundary-layer transition", *NACA T. N. No.* 3489, 1955.

Speziale, C. G., & Mac Giolla Mhuiris, N. (1989). On the prediction of equilibrium states in homogenous turbulence. *J. Fluid Mech.*, 209, 591-615.

Speziale, C. G. (1979). Invariance of turbulence closure models. *Phys. Fluids*, 22 1033.

Speziale, C. G. (1987). On non-linear K-l and K- $\epsilon$  models of turbulence. *J. Fluid Mech.*, 178, 459.

Speziale, C. G. (1989). Turbulence modeling in non-inertial frames of reference. *Theoret. Comput. Fluid Dynamics*, 1, 3-19.

Speziale, C.G., Sarkar S. & Gatski T.B. (1991). Modeling the pressure strain correlation of turbulence : an invariant dynamical systems approach. *J. Fluid Mech.*, 227, 245-272.

Y. B. Suzen & P. G. Huang, "Modeling of Flow Transition Using an Intermittency Transport Equation", *J. Fluids Eng.* **122** (6), pp. 273-284, 2000.

H. -S. Tsuei & J. B. Perot, "Turbomachinery Predictions Using the Turbulent Potential Model", *AIAA 2000-0135*, Reno, Nevada, Jan, 2000

S. Turek, "Tools for simulating non-stationary incompressible flow via discretely divergence-free finite element models", *Int. J. Numer. Meth. Fluids*, **18**, pp. 71-105 ,1994.

Wallin, S., & Girimaji, S.S. (2000). Evolution of an isolated turbulent trailing vortex *AIAA Journal*, 38, (4), 657-665

Z. U. A. Warsi, *Fluid Dynamics Theoretical and Computational Approaches*, CRC Press LLC, Florida, 1999

C. S. Well, "Effects of Free stream Turbulence on Boundary Layer Transition," *AIAA J.*, **5** (1), pp. 172-174, 1967

F. M. White, *Viscous Fluid Flow*, McGraw-Hill, 199.

Wigeland, R. A. & Nagib, H. M. (1978). Grid generated turbulence with and without rotation about the streamwise direction. IIT Fluids and Heat Transfer Rep. R78-1, Illinois Inst. Of Tech., Chicago, Illinois.

E. R. Van Driest & C. B. Blumer, "Boundary Layer Transition, Freestream Turbulence, and Pressure Gradient Effects", *AIAA J.*, **1**, pp. 1303-1306, 1963.

J. Van Kan, "A second order accurate pressure-correction scheme for viscous incompressible flow", *SIAM J. Sci. Comput.*, **7**, pp. 870-891 1986.

X. Zhang & J. B. Perot, "Unsteady Flow Prediction of Turbulent Flow Around a Triangular Cylinder", *FEDSM 2000-11172*, Boston, MA, June, 2000

X. Zhang, D. Schmidt & J. B. Perot, "Accuracy and conservation properties of a three-dimensional staggered mesh scheme", *J. Comput. Phys.*, **175**, pp. 764-791 2002.